Design and Analysis

of

Stop-Rotor Multimode Unmanned Aerial Vehicle (UAV)

by

Alvaro Vargas-Clara

A Thesis in Partial Fulfillment
of the Requirements for the Degree
Master of Science in Technology

Approved July 2011 by the
Graduate Supervisory Committee:

Sangram Redkar, Chair
Narciso Macia
John Rajadas

ARIZONA STATE UNIVERSITY

August 2011

ABSTRACT

The objective of this work is to develop a Stop-Rotor Multimode UAV. This UAV is capable of vertical take-off and landing like a helicopter and can convert from a helicopter mode to an airplane mode in mid-flight. Thus, this UAV can hover as a helicopter and achieve high mission range of an airplane. The stop-rotor concept implies that in mid-flight the lift generating helicopter rotor stops and rotates the blades into airplane wings. The thrust in airplane mode is then provided by a pusher propeller. The aircraft configuration presents unique challenges in flight dynamics, modeling and control. In this thesis a mathematical model along with the design and simulations of a hover control will be presented. In addition, the discussion of the performance in fixed-wing flight, and the autopilot architecture of the UAV will be presented. Also presented, are some experimental "conversion" results where the Stop-Rotor aircraft was dropped from a hot air balloon and performed a successful conversion from helicopter to airplane mode.

i

DEDICATION

I dedicate my Master's thesis to my inspirational and supporting mentor, Dr. Sangram Redkar, and my parents who have made this possible with all their support, sacrifice and love, Mr. Fernando Vargas Briones and Mrs. Blanca Clara de Vargas.

ACKNOWLEDGMENTS

TABLE OF CONTENTS

CHAPTER

LIST OF TABLES

LIST OF FIGURES

Chapter 1

INTRODUCTION

1.1   History of Aviation

Humankind has demonstrated the interest and ambition in flight since the early

ages of civilization. Early attempts of flight, date back as early as 200 B.C.

through the use of a kite (Brown, 1922). Attempts of flight progressed to different

forms of flight through the use of kites, balloons, gliders, powered heavier-than-

air, supersonic and spaceflights (Crouch, 2004). Better understanding, innovations

and technology have contributed to the progression of human aviation. In some

instances the progress of aviation has been halted to a grind. For instance the

Wright Brothers achieved successful powered heavier-than-air flight because they

solved the critical issue of roll control, although most people believe that it was

the recognition of the simplification offered by separating lift from propulsion

which was already recognized since Sir George Cayley's time. Yaw and pitch

control were already resolved by Cayley's cruciform rudder. But the remaining

critical issue of roll control was not practically solved by Otto Lilienthal and

others using shifting weight. Successful powered heavier-than-air flight was not

possible until the Wrights solved roll control with wing warping. Fixed-wing

aircraft performance has since far eclipsed those humble beginnings. Similarly,

rotary wing developments have also far eclipsed the modest flight performances

pioneered by Sikorsky, Piasecki and others.

1.2   Ideal Aircraft

Airplanes are unquestionably the supreme aircraft for any meaningful payload,

speed and range, although they require the use of runways. On the other hand, helicopters are without doubt the most versatile aircraft, featuring no need for runways, but cannot compare to fixed-wing aircraft for payload, speed, and range. A 'multimode' vehicle that would be as versatile as a helicopter but enjoy the payload, speed and range of an airplane would be an ideal aircraft.

1.3   Literature Search

1.3.1   Tilt-Rotor Aircraft

There have been countless attempts to create such aircraft. But most have fail to accomplish this in the most effective and efficient manner. For instance the rotors on tilt-rotor vehicle, such as the V-22 Osprey and the TR911D Eagle Eye UAV, are necessarily fundamentally compromised in terms of blade twist, geometry, et cetera, due to conflicting requirements depending on the mode of flight (Drier, 2007). In cruise as a fixed-wing, the rotors are far from ideal as a thrust device; and while in helicopter mode, the rotors are likewise far from ideal in hover and particularly in autorotation. Such fundamental compromises will likely make a candidate small tilt-rotor, Vertical Take Off and Landing (VTOL), UAV performance fall well short of the range and endurance performance objectives over fixed-wing (citing the Scan Eagle example) and gain the VTOL capability. For over five decades, the aerospace community has recognized that such an ideal aircraft would likely be a stop-rotor configuration.

1.3.2   Stop-Rotor Concept

The Stop-Rotor studied here has the VTOL and fixed-wing flight capabilities similar to a tilt-rotor aircraft. The main difference between a tilt-rotor aircraft and

2

stop-rotor is that the rotor that provides lift in VTOL mode is stopped in midflight and it is then used as a lift surface in fixed-wing flight mode. For most of those five decades, countless stop-rotor concepts and ideas have been advanced. Among recent efforts have been the cancelled, Boeing X-50 Canard Rotor Wing and the Sikorsky X-Wing as shown in Figure 1.1.

Figure 1.1. **Stop-rotor aircrafts the X-50 Canard Rotor (left and middle) and Sikorsky X-Wing (right)**

1.3.3   Radial Flow Stop-Rotor

In virtually every case known to the author, the stop-rotor concepts were of a radial flow conversion category. This is to say the rotor disc is parallel to the air flow during conversion when the rotors are to be slowed and stopped to become wings. A radial flow conversion stop-rotor forces the airfoil to experience approximately 180º change in direction of the airflow on the airfoil during conversion between rotary and fixed-wing flight modes. This is because on the retreating blade side, the rotor's trailing edge becomes a leading edge when locked in the fixed-wing position. This has resulted in very serious compromises and consequences including 50% chord-wise pitching axis placement; creating considerable aero-elasticity problems including flutter, and a one per revolution oscillatory center of lift during conversion. All of these and other problems and

similar challenges encountered have proven to be virtually undefeatable by radial flow conversion stop-rotor design approaches.

Like the roll control, critical issues plaguing airplane developers fifty years since Cayley's experiments, the stop-rotor development progress has been stalled for fifty years mainly over the obstacle of the conversion approach between rotary and fixed-wing flight modes. What is evidently needed to resolve this critical issue hampering stop-rotor development is a departure from the radial flow conversion approach.

1.3.4   Axial Flow Stop-Rotor

Axial flow conversion is analogous to feathering or pitching propellers with the airflow impinging upon the rotor disc plane perpendicularly, aligned with the rotational axis of the rotor. The principal advantage of an axial flow conversion approach compared to the radial flow conversion is the airflow impinging the airfoil does not change direction, so the airfoil can have conventional, normal profiles with aero-elastically stable quarter chord pitch axes. In this work, we focus on an axial stop-rotor. We present the theoretical as well as experimental results, performance, stability and structural stress analysis of this aircraft.

1.4   Stop-Rotor UAV Project

The Stop-Rotor UAV proposed herein, is the first and only stop-rotor concept where an axial flow conversion approach is advanced. The Stop-Rotor UAV comprises of four major components: fuselage, wings, tail rotor and push propeller. Figure 1.2 illustrates these components in both helicopter and airplane mode (Vargas-Clara, 2010).
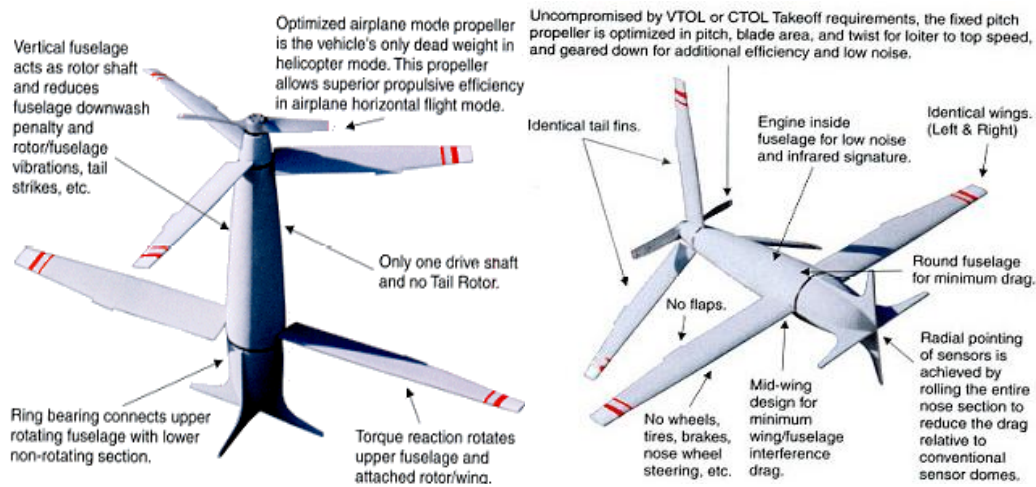
Figure 1.2. **Stop-Rotor UAV in helicopter (left) and airplane mode**

(right)

The fuselage accommodates the engine, rotor shaft, clutch and any electrical and navigational hardware. The wings are a conventional NACA 0012 airfoil. In helicopter mode the wings are feathered and act as a rotor to counteract the torque from the tail rotor, while in airplane mode they act like conventional fixed-wings. The tail rotor also consists of a NACA 0012 airfoil. In helicopter the tail rotor is the sole lift generating mechanism and is the only powered rotor. In airplane mode the clutch disengages power to the tail rotor and the tail rotor is feathered and assumes the role of a tail in conventional fixed-wing aircraft. The final main component of the Stop-Rotor UAV is the push propeller; its sole purpose is to provide thrust in airplane mode. The push propeller is optimized in pitch, blade area and twist to provide the best performance of speed, range and endurance.

The flight conversion concept for the Stop-Rotor UAV is illustrated in Figure 1.3. It is important to note that the Stop-Rotor UAV can convert between helicopter and airplane modes any number of times during the same flight. The

5

helicopter mode is not just the launch and recovery method.
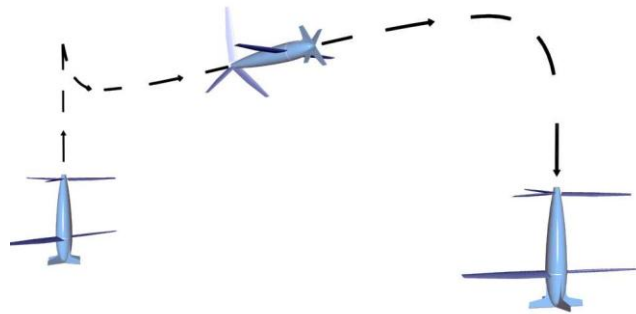
Figure 1.3. **Stop-Rotor UAV flight conversion**

Conceptually, the conversion from powered helicopter to airplane mode can be achieved by releasing a selectable clutch while the wings and tail fins are collectively pitched (analogous to feathering a propeller) until it is in the airplane mode position. The wings and tail fins stop rotating solely due to external aerodynamic forces and do not require indexing or braking. The selectable clutch engages the propeller drive shaft and power is now delivered to the pusher propeller for airplane flight mode. The propeller is thus optimized for cruise and not compromised like so many fixed pitch propeller UAVs for take-off and cruise conditions. For the conversion from airplane to helicopter mode the clutch is released and the wing and tail fins are collectively pitched to the auto rotating position. The wings and tail fins spin up solely due to external aerodynamic forces. The selectable clutch engages the tail rotor hub and power is then delivered to the tail rotor for powered helicopter flight mode while the collective pitch is increased to provide hovering and normal helicopter-like flight functionalities.

Thus, the Stop-Rotor UAV is an ideal fixed-wing, uncompromised in terms of propulsion and landing mechanism making available higher weight

fractions for payload and fuel for longer endurance and greater payload than conventional fixed-wing. In helicopter mode, Stop-Rotor UAV is an ideal rotary wing vehicle, with efficient, slow turning rotors without the need of power-robbing tail rotor for anti-torque.

1.5   Scope of Project

The scope of the project includes creating a mathematical model of the Stop-Rotor UAV. This model will then be used to conduct simulations so as to aid the development of the Stop-Rotor UAV, controller design and implementation to control the states in hover flight. In addition, a proof of concept drop test is to be conducted to prove that the Stop-Rotor UAV can efficiently convert between the flight-modes. In the drop test, the objective is to gather data, which will be used to compare experimental results to the simulation results. Furthermore, fixed-wing aircraft configuration is to be analyzed, to study the stability and performance of the Stop-Rotor UAV.

1.6   Organization of the Thesis

It is noted that this work was funded by the US Navy. ASU was tasked with specific milestones and Work Breakdown Schedule (WBS). ASU was responsible for:

a) Developing mathematical model and proposing control strategies in pure hover.

b) Instrumenting a stop rotor specimen for the big drop to validate the multimode capability of the Stop-Rotor UAV.

c) Analyze the data from the big drop and correlate the results with simple, first order model and develop transition equations.

d) Perform preliminary analysis of the stop rotor stability in the airplane mode and conduct stress analysis to check if the wing structure could sustain the loads and stress during the big drop.

This thesis follows the same outline as the WBS and the progress notes submitted to the Navy. While the significant part of thesis is devoted to the development of mathematical model and controller design, other work done during the project are also included in the thesis and constitute chapters three and four. Even though the tasks (or the chapters in this thesis) may not seem to be tightly linked they fit in the big picture and are required for developing a completely autonomous multimode Stop-Rotor UAV.

Chapter 1 presents brief introduction and the literature review. The mathematical model of the Stop-Rotor UAV in hover flight is discussed in Chapter 2, along with some strategies for the hover control. Control robustness is discussed in this chapter as well. Chapter 3 presents the experimental 'proof of concept test' showing the transition from rotary wing to fixed-wing. The preliminary equations for transition dynamics are also derived in this chapter. Chapter 4 has the basic fixed-wing stability and wing structure stress analysis. Chapter 5 has discussions and conclusion.

Chapter 2

MATHEMATICAL MODEL AND CONTROL FOR HOVER FLIGHT

In this chapter, a mathematical model of the Stop-Rotor UAV will be presented.

This model will allow for the comparison of linear and nonlinear controls

techniques and tune various parameters and controller gains. In addition, control

robustness will be discussed. This model will give an insight of the aircraft's

stability, controllability and flight dynamics. The mathematical model will

primarily focus on dynamics of the aircraft in hover flight.

2.1 Mathematical Model

The Stop-Rotor UAV in hover flight is similar to a coaxial helicopter. It

comprises of two contra-rotating rotors. The tail rotor is supplying thrust in hover

flight while the wing rotor is simply counter rotating due to the counter torque.

However, the main differences between the stop rotor configuration and the

coaxial helicopter are:

1. In case of the coaxial helicopter, both the rotors are powered and are in close

proximity. Thus, the *bottom* rotor is in the 'down wash' of the top rotor. In the

case of the stop-rotor the *bottom* (wing) rotor rotates purely due to anti-torque.

2. In the case of a stop-rotor, the top (tail) rotor and the *bottom* (wing) rotor are

separated by the fuselage and hence the top rotor 'down wash' effects are not as

significant as the coaxial helicopter.

3. Unlike the coaxial helicopter, where top and *bottom* rotors produce significant

amount of thrust, the stop-rotor top (tail) rotor contributes to the majority of

thrust.

The stop-rotor is shown in Figure 2.1 along with the coordinate systems used to derive the equations of motion.
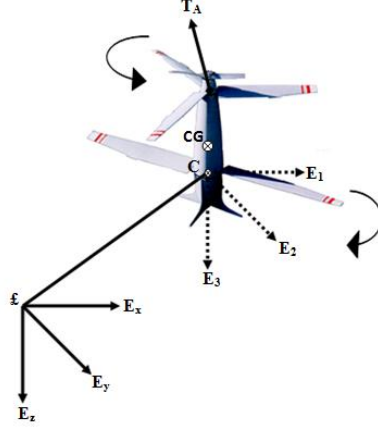
Figure 2.1. **Stop Rotor UAV model representation**

£ = {E_x, E_y, E_z} as a right hand inertial frame, which is stationary with respect to the earth. Let C = {E_1, E_2, E_3} be a right hand body fixed frame, where CG is the fixed position center of mass of the aircraft. **R** , is an orthogonal rotation matrix. **R** : C→£ denotes the aircraft orientation with respect to £. Where ψ, θ, ϕ describes yaw, pitch, and roll angles respectively. The rotational matrix that aligns the body fixed frame to the inertial frame is given by

$$\mathbf{R}(\psi,\theta,\phi) = \begin{pmatrix} c_\phi c_\psi & s_\phi s_\theta c_\psi - c_\phi s_\psi & c_\phi s_\theta c_\psi + s_\phi s_\psi \\ c_\theta s_\psi & s_\phi s_\theta s_\psi + c_\phi c_\psi & c_\phi s_\theta s_\psi - s_\phi s_\psi \\ -s_\theta & s_\phi c_\theta & c_\phi c_\theta \end{pmatrix} \qquad (2.1)$$

where $c_\theta = \cos\theta$ and $s_\theta = \sin\theta$

Dynamic model was obtained by with the following assumptions:

- The blades of the two rotors are not hinged, but are directly attached to the hub. As a consequence each rotor blades will always lie in a disk termed

10

rotor disk.

- The tail rotor, denoted by 'A' for *above* rotor, is assumed to rotate in an anti-clockwise direction when viewed from above. The wing rotor, denoted by 'B' for *bottom* rotor, rotates in a clockwise direction.

- It is assumed that the cyclic lateral and longitudinal tilts of the tail rotor disk are measureable and controllable. The tail rotor is the only rotor that has inputs for flapping angles.

- The only air resistances modeled are simple drag forces opposing the rotation of the two rotors.

- Aerodynamic forces generated by the relative wind are not considered

- The interaction of the ground and aircraft is neglected.

- The interaction of the two rotors acting in close proximity will not be considered.

For simplification, the model will be split into two major sections. First section will cover the translational forces acting on the aircraft. The second section will cover the rotational dynamics. A complete model will then be presented that will combine these two sections.

2.1.1 Translational Forces

The forces acting on the fuselage of the aircraft are the forces produced by the *above* rotor, *bottom* rotor and lastly due to gravity. Denoted by T_A the thrust generated by the *above* 'A' (Tail) rotor while denoted T_B the thrust generated by the *bottom* 'B' (Wing) rotor. The thrust of the *above* and *bottom* rotor are described as the following:

$$T_A = T_A^1 E_1 + T_A^2 E_2 - T_A^3 E_3 \qquad (2.2)$$

$$T_B = T_B^1 E_1 + T_B^2 E_2 - T_B^3 E_3 \qquad (2.3)$$

Since the *bottom* rotor has no swash plate. The thrust vector of this rotor only has the same direction, i.e. in the direction of the E_3 axis, so Equation (2.3) can be rewritten:

$$T_B = -T_B^3 E_3 \qquad (2.4)$$

As described in (Castillo et al., 2004), the thrust vector for the *above* rotor is defined as a function of the flapping angle β. The angle represents the tilt of the *above* rotor disk with respect to its initial rotation plane. This angle consists of angle *a* (longitudinal flapping) and angle *b* (lateral flapping) in which they were assumed to be measureable and controllable variables. Figure 2.2 illustrates this correlation.
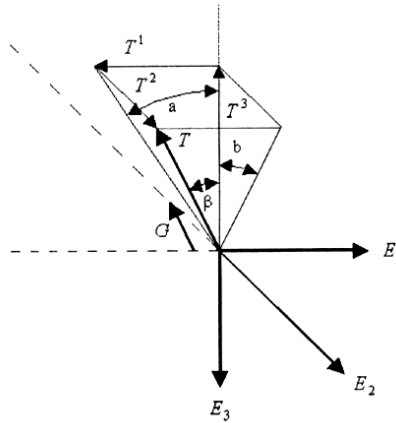
Figure 2.2. **Thrust vector of *above* (tail) rotor (Castillo et al., 2004)**

Using geometric calculus, the projection of the thrust components of T_A can be expressed as:

$$T_A^1 = \frac{-\sin(a)\cdot\cos(b)}{\sqrt{1-\sin^2(a)\cdot\sin^2(b)}}\cdot|T_A| \tag{2.5}$$

$$T_A^2 = \frac{\cos(a)\cdot\sin(b)}{\sqrt{1-\sin^2(a)\cdot\sin^2(b)}}\cdot|T_A| \tag{2.6}$$

$$T_A^3 = \frac{-\cos(a)\cdot\cos(b)}{\sqrt{1-\sin^2(a)\cdot\sin^2(b)}}\cdot|T_A| \tag{2.7}$$

The thrust vector T_A can be expressed as

$$T_A = G(a,b)\cdot|T_A| \tag{2.8}$$

where,

$$G(a,b) = \frac{1}{\sqrt{1-\sin^2(a)\cdot\sin^2(b)}}\cdot\begin{pmatrix} -\sin(a)\cdot\cos(b) \\ \cos(a)\cdot\sin(b) \\ -\cos(a)\cdot\cos(b) \end{pmatrix} \tag{2.9}$$

Lastly, the final force applied to the Stop-Rotor UAV is gravitational force given by:

$$f_g = mgE_z \tag{2.10}$$

where, m defines the total mass of the aircraft and g is the gravity constant.

Equation (2.10) is given in the inertial fixed frame £.

So the external total force applied to the aircraft can be represented by F:

$$F = T_A + T_B + f_g \tag{2.11}$$

$$F = \mathbf{R}G(a,b)\cdot|T_A| - \mathbf{R}T_B^3 E_3 + mgE_z \tag{2.12}$$

This is the representation of F on the inertial frame.

2.1.2 Torques and Anti-Torques

Due to the thrusts T_A and T_B the torques will be generated. The torques are due to

13

the separation between the center of mass (CG) and the rotor hubs. τ_A and τ_B are denoted as the torques produced by T_A and T_B respectively.

Represented by l_A and l_B are the measured distances from the CG to the hubs of the *above* and *bottom* rotor respectively. So the torques being applied to the aircraft are:

$$\tau_A = l_A \times T_A \tag{2.13}$$

$$\tau_B = l_B \times T_B \tag{2.14}$$

In addition, the aerodynamic drags acting on the rotors produce pure torques acting through the rotor hubs. So the anti-torques are defined by:

$$Q_A = |Q_A| E_3 \tag{2.15}$$

$$Q_B = -|Q_B| E_3 \tag{2.16}$$

Lastly, the total torque applied to the aircraft can be expressed in the body fixed frame as:

$$\tau = \tau_A + \tau_B + |Q_A| E_3 - |Q_B| E_3 \tag{2.17}$$

2.1.3 Complete Dynamic Model

By incorporating the total forces and total torques, the following complete dynamic model is obtained in the inertial frame:

$$\dot{\xi} = v \tag{2.18}$$

$$m\dot{v} = RG(a,b) \cdot |T_A| - T_B^3 R E_3 + mg E_z \tag{2.19}$$

$$\dot{R} = R\hat{\Omega} \tag{2.20}$$

$$I\dot{\Omega} = -\Omega \times I\Omega + \tau_A + \tau_B + |Q_A|E_3 - |Q_B|E_3 \tag{2.21}$$

In the translation movement of the aircraft, let $\dot{\xi}$ (c.f. Equation (2.18)) define the velocity, v, of the aircraft's CG expressed in its inertial frame £. In Newton's

equations of motion $I\dot{\Omega} = -\Omega \times I\Omega + \tau$ denotes the rotational component of movement in a non-inertial frame, where Ω is the angular velocity in the non-inertial frame; I defines the inertia of the aircraft in its CG in respect to the body fixed frame and τ represents the total external torque applied in the body fixed frame.

Also it is important to define that $\Omega \in |R^3$ and

$$\hat{\Omega} = \begin{pmatrix} 0 & -\Omega^3 & \Omega^2 \\ \Omega^3 & 0 & -\Omega^1 \\ -\Omega^2 & \Omega^1 & 0 \end{pmatrix} \tag{2.22}$$

The mathematical model presented above embodies the dynamics of the aircraft in vector form, but to conduct simulations and analyze the dynamics of the aircraft this model will be expanded using Newton-Euler formulation, which will be presented in the following section.

2.1.4 The Detailed Mathematical Model

The Newton model will be expanded to Newton-Euler form to code and simulate the dynamics of the aircraft in hover flight. The Newton-Euler model is expanded using the same assumptions, and equations previously stated in previous sections as well as using Figure 2.1 as aircraft model representation. The main objective for expanding the model is to be able to implement it in a MATLAB code and simulate to obtain translation and rotational dynamics of the aircraft. This model expansion will be split into two parts, one covering the translation dynamics and the other the rotational dynamics.

For the expanded model, let define $\mathbf{R_{exp}}$ as:

$$\mathbf{R}_{\exp}(\phi,\theta,\psi) = \begin{pmatrix} c_\psi c_\theta & c_\psi s_\theta s_\phi - s_\psi c_\phi & c_\psi s_\theta c_\phi + s_\psi s_\phi \\ s_\psi c_\theta & s_\psi s_\theta s_\phi + c_\psi c_\phi & s_\psi s_\theta c_\phi - s_\phi c_\psi \\ -s_\theta & s_\phi c_\theta & c_\phi c_\theta \end{pmatrix} \tag{2.23}$$

where $c_\theta = \cos(\theta)$ and $s_\theta = \sin(\theta)$ are used as before.

$\mathbf{R}_{\exp}$ is an orthogonal rotation matrix. $\mathbf{R}_{\exp}$: C→£ denotes the aircraft orientation with respect to £.

The translation dynamics for the expanded Newton-Euler model (Bouabdallah, 2010) in the fixed inertial frame £ are:

$$\ddot{E}_X = \frac{1}{m} \cdot \left[\left(c_\psi c_\theta\right) \cdot \left(T_A^1\right) + \left(s_\psi c_\phi + c_\psi s_\theta s_\phi\right) \cdot \left(T_A^2\right) + \left(c_\psi s_\theta c_\phi + s_\psi s_\phi\right) \cdot \left(T_A^3 - T_B\right) \right] \tag{2.24}$$

$$\ddot{E}_Y = \frac{1}{m} \cdot \left[\left(s_\psi c_\theta\right) \cdot \left(T_A^1\right) + \left(s_\psi s_\theta s_\phi + c_\psi c_\phi\right) \cdot \left(T_A^2\right) + \left(s_\psi s_\theta c_\phi + s_\phi c_\psi\right) \cdot \left(T_A^3 - T_B\right) \right] \tag{2.25}$$

$$\ddot{E}_Z = g + \frac{1}{m} \cdot \left[\left(s_\theta\right) \cdot \left(T_A^1\right) + \left(s_\phi c_\theta\right) \cdot \left(T_A^2\right) + \left(c_\phi c_\theta\right) \cdot \left(T_A^3 - T_B\right) \right] \tag{2.26}$$

The expansion of the rotational dynamics in the Newton-Euler's model uncovers the body gyro-effect, rotor gyro-effect, inertial-counter torque and counter torque unbalance which were all hidden in the Newton model. So the rotational dynamics for the expanded model in the fixed inertial frame £ are:

$$I_{xx}\ddot{\phi} = \dot{\theta}\dot{\psi}\left(I_{yy} - I_{zz}\right) - J_B\dot{\theta}\Omega_B + J_A\dot{\theta}\Omega_A + T_A^2 l_A \tag{2.27}$$

$$I_{yy}\ddot{\theta} = \dot{\phi}\dot{\psi}\left(I_{zz} - I_{xx}\right) + J_B\dot{\phi}\Omega_B - J_A\dot{\phi}\Omega_A + T_A^1 l_A \tag{2.28}$$

$$I_{zz}\ddot{\psi} = \dot{\phi}\dot{\theta}\left(I_{xx} - I_{yy}\right) + Q_A - Q_B \tag{2.29}$$

where I_{xx}, I_{yy}, I_{zz} are the moments of inertia of the aircraft about the CG; $J_{A/B}$ are the rotor inertias of the *above* and *bottom* rotor respectively.

16

To obtain the thrust (T) and drag moment (Q) for the *above* and *bottom* rotor, the momentum theory is used, which is discussed in the following section.

2.1.5   Rotor Aerodynamics

For any airfoil at a certain angle of attack it will produce a lift force and drag force. This is true for a rotor since it basically consists of airfoils pinned at a one end and rotating about the pinned end. In analyzing the two rotors, we can obtain the lift and drag forces as (Drier, 2007):

$$dL = C_L \cdot \frac{1}{2} \cdot \rho \cdot (\Omega \cdot r)^2 \cdot c \cdot dr \tag{2.30}$$

$$dD = C_D \cdot \frac{1}{2} \cdot \rho \cdot (\Omega \cdot r)^2 \cdot c \cdot dr \tag{2.31}$$

where C_L and C_D are the lift and drag coefficients respectively; ρ is the density of air; r is radius location of the blade and c is the chord length of the blade.

Since the objective is to obtain the vertical thrust and horizontal drag moment produced by blades both thrust and drag force have components in the vertical thrust since the blade is pitch at angle $\hat{\phi}$ illustrated in Figure 2.3.
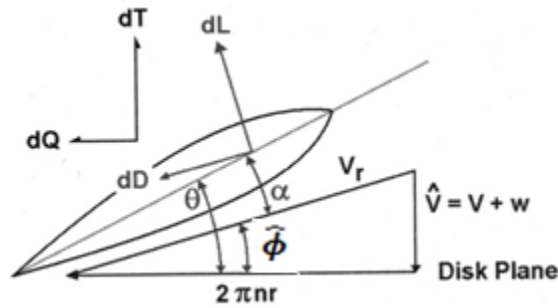
***Figure 2.3.* Blade section view**

Therefore, thrust force and drag moment are the following:

$$dT = dL \cdot \cos(\hat{\phi}) - dD \cdot \sin(\hat{\phi}) \tag{2.32}$$

17

$$dQ = (dL \cdot \sin(\hat{\phi}) + dD \cdot \cos(\hat{\phi}))r \tag{2.33}$$

Substitute dL and dD into both dT and dQ and integrate with respect to the blade radius we obtain:

$$T_A = \frac{1}{6} C_L \cdot \rho \cdot \Omega_A^2 \cdot c_A \cdot R_A^3 \cos(\hat{\phi}) - \frac{1}{6} C_D \cdot \rho \cdot \Omega_A^2 \cdot c_A \cdot R_A^3 \sin(\hat{\phi}) \tag{2.34}$$

Equation (2.34) is thrust force for a single blade of the *above* rotor. We can obtain the total thrust force produced by the *above* rotor by multiplying the equation by the number of blades, *n*, in the rotor.

$$T_A = \left(\frac{1}{6} C_L \cdot \rho \cdot \Omega_A^2 \cdot c_A \cdot R_A^3 \cos(\hat{\phi}) - \frac{1}{6} C_D \cdot \rho \cdot \Omega_A^2 \cdot c_A \cdot R_A^3 \sin(\hat{\phi}) \right) \cdot n \tag{2.35}$$

where *n* is 3, or 2 for either the *above* or *bottom* rotor respectively.

The drag moment for both *above* and *bottom* rotor is the following:

$$Q = \left(\frac{1}{8} C_L \cdot \rho \cdot \Omega^2 \cdot c \cdot R^4 \sin(\hat{\phi}) + \frac{1}{8} C_D \cdot \rho \cdot \Omega^2 \cdot c \cdot R^4 \cos(\hat{\phi}) \right) \cdot n \tag{2.36}$$

To obtain the value of angular velocity, Ω_A for the *above* rotor the trim condition during hover flight is used:

$$T_A = mg \tag{2.37}$$

Solve for Ω_A

$$\Omega_A = \sqrt{\frac{mg}{\frac{1}{2} C_L \cdot \rho \cdot c_A \cdot R_A^3 \cos(\hat{\phi}) - \frac{1}{2} C_D \cdot \rho \cdot c_A \cdot R_A^3 \sin(\hat{\phi})}} \tag{2.38}$$

To obtain the value of angular velocity, Ω_B for the *bottom* rotor the following condition is used:

$$Q_A - Q_B = J\ddot{\theta} \tag{2.39}$$

18

Since in steady hover $\ddot{\theta}$ is zero, Equation (2.39) results into the following:

$$Q_A = Q_B \tag{2.40}$$

To solve for the angular velocity, Ω_B for the *bottom* rotor we solve Equation (2.40) for Ω_B that makes the condition (2.40) true. So Ω_B is the following:

$$\Omega_B = \sqrt{\frac{3}{2} \cdot \frac{\Omega_A^2 \cdot c_A \cdot R_A^4}{c_B \cdot R_B^4}} \tag{2.41}$$

This concludes the mathematical model for the Stop–Rotor UAV. The next section will discuss possible control options for controlling the states in the hover flight.

2.2   Controller Design for Hover flight

In this section, three control systems will be created and implemented to the nonlinear rotational dynamics described in the previous chapter. The three control systems consist of a linear controller, optimal linear controller and a nonlinear controller. Their main objective here is to stabilize the rotational dynamics of the system.

2.2.1   Linear Controller

First, to create a linear controller for a nonlinear system the system had to be linearized about an equilibrium solution. The linearized equations of motion take form of:

$$\ddot{\phi} = \left(\frac{1}{I_{xx}}\right)\left(-J_B\dot{\theta}\Omega_B + J_A\dot{\theta}\Omega_A + T_A^2 l_A\right) \tag{2.42}$$

$$\ddot{\theta} = \left(\frac{1}{I_{yy}}\right)\left(J_B\dot{\phi}\Omega_B - J_A\dot{\phi}\Omega_A + T_A^1 l_A\right) \tag{2.43}$$

19

$$\ddot{\psi} = \left(\frac{1}{I_{zz}}\right)(Q_A - Q_B) \tag{2.44}$$

To control the rotational dynamics the system command inputs have been included in roll, pitch, and yaw to stabilize the dynamics. With addition of the command inputs the linearized state equations take the following form:

$$\ddot{\phi} = \left(\frac{1}{I_{xx}}\right) \cdot (-J_B \cdot \dot{\theta} \cdot \Omega_B + J_A \cdot \dot{\theta} \cdot \Omega_A + T_{act\,Roll}) \tag{2.45}$$

$$\ddot{\theta} = \left(\frac{1}{I_{yy}}\right) \cdot (J_B \cdot \dot{\phi} \cdot \Omega_B - J_A \cdot \dot{\phi} \cdot \Omega_A + T_{act\,Pitch}) \tag{2.46}$$

$$\ddot{\psi} = \left(\frac{1}{I_{zz}}\right) \cdot (T_{act\,Yaw}) \tag{2.47}$$

where, $T_{act\,Roll}$, $T_{act\,Pitch}$, and $T_{act\,Yaw}$ are command inputs for roll, pitch, and yaw respectively. The next step for linearization of the system is to convert it to state-space form.

$$\frac{d}{dt}\begin{Bmatrix} \phi \\ \dot{\phi} \\ \theta \\ \dot{\theta} \\ \psi \\ \dot{\psi} \end{Bmatrix} = \begin{bmatrix} 0 & 1 & 0 & 0 & 0 & 0 \\ 0 & 0 & 0 & \dfrac{-J_B\Omega_B + J_A\Omega_A}{Ixx} & 0 & 0 \\ 0 & 0 & 0 & 1 & 0 & 0 \\ 0 & \dfrac{J_B\Omega_B + J_A\Omega_A}{Iyy} & 0 & 0 & 0 & 0 \\ 0 & 0 & 0 & 0 & 0 & 1 \\ 0 & 0 & 0 & 0 & 0 & 0 \end{bmatrix} \begin{Bmatrix} \phi \\ \dot{\phi} \\ \theta \\ \dot{\theta} \\ \psi \\ \dot{\psi} \end{Bmatrix} \tag{2.48}$$

The system (2.48) has been now linearized. By analyzing the equations in yaw and rate of yaw, one can conclude that yaw is independent of roll and pitch, but roll and pitch are dependent on upon each other. The linear controller will be of the following form:

$$\dot{\mathbf{x}} = \mathbf{A}\mathbf{x} + \mathbf{B}u(t) \tag{2.49}$$

where, $\dot{x}$ is a state rate, $\mathbf{A}$ is the state matrix, $\mathbf{B}$ is the controller matrix and, $\mathbf{u}(t)=\mathbf{Kx}$ in which $\mathbf{K}$ is a matrix of control gains.

$$\mathbf{A} = \begin{bmatrix} 0 & 1 & 0 & 0 & 0 & 0 \\ 0 & 0 & 0 & \dfrac{-J_B\Omega_B + J_A\Omega_A}{Ixx} & 0 & 0 \\ 0 & 0 & 0 & 1 & 0 & 0 \\ 0 & \dfrac{J_B\Omega_B + J_A\Omega_A}{Iyy} & 0 & 0 & 0 & 0 \\ 0 & 0 & 0 & 0 & 0 & 1 \\ 0 & 0 & 0 & 0 & 0 & 0 \end{bmatrix} \tag{2.50}$$

$$\mathbf{B} = \begin{bmatrix} 0 & 0 & 0 & 0 & 0 & 0 \\ 1 & 1 & 0 & 0 & 0 & 0 \\ 0 & 0 & 0 & 0 & 0 & 0 \\ 0 & 0 & 1 & 1 & 0 & 0 \\ 0 & 0 & 0 & 0 & 0 & 0 \\ 0 & 0 & 0 & 0 & 1 & 1 \end{bmatrix} \tag{2.51}$$

$$\mathbf{K} = \begin{bmatrix} K1 & K2 & K3 & K4 & K5 & K6 \\ K7 & K8 & K9 & K10 & K11 & K12 \\ K13 & K14 & K15 & K16 & K17 & K18 \\ K19 & K20 & K21 & K22 & K23 & K24 \\ K25 & K26 & K27 & K28 & K29 & K30 \\ K31 & K32 & K33 & K34 & K35 & K36 \end{bmatrix} \tag{2.52}$$

With the above assumption the controller would be of the form $\mathbf{B} \cdot \mathbf{Kx}$ giving the following state control inputs of:

$$\begin{aligned} T_{act_{Roll}} &= K_1\phi + K_2\dot{\phi} + K_3\theta + K_4\dot{\theta} \\ T_{act_{Pitch}} &= K_5\phi + K_6\dot{\phi} + K_7\theta + K_8\dot{\theta} \\ T_{act_{Yaw}} &= K_9\psi + K_{10}\dot{\psi} \end{aligned} \tag{2.53}$$

where:

$$K_1 = K1 + K7$$
$$K_2 = K2 + K8$$
$$K_3 = K3 + K9$$
$$K_4 = K4 + K10$$
$$K_5 = K13 + K19$$
$$K_6 = K14 + K20 \qquad (2.54)$$
$$K_7 = K15 + K21$$
$$K_8 = K16 + K22$$
$$K_9 = K29 + K35$$
$$K_{10} = K30 + K36$$

The approach here would be to determine the gains in the matrix $\mathbf{K}$ that would give all negative real parts for the eigenvalues for the matrix $[\mathbf{A} - \mathbf{BK}]$. This proved to be rather challenging since the characteristic polynomial was extremely intricate and long. The strategy was to obtain the characteristic polynomial to be of the form:

$$a_0\lambda^6 + a_1\lambda^5 + a_2\lambda^4 + a_3\lambda^3 + a_4\lambda^2 + a_5\lambda + a_6 \qquad (2.55)$$

Then using the stability criteria of Routh-Hurwitz and Lienard-Chipart to obtain conditions for the gains that would give all negative real parts for the eigenvalues of matrix $[\mathbf{A} - \mathbf{BK}]$. This proved rather complicated and yielded multiple solutions. One of the possible solutions was to use rate and state feedback type controller with

$$K_3 = 0$$
$$K_4 = 0$$
$$K_5 = 0 \qquad (2.56)$$
$$K_6 = 0$$

With the above assumption the state control inputs in Equation (2.53) will be reduced to the following:

$$T_{act_{Roll}} = K_1\phi + K_2\dot{\phi}$$
$$T_{act_{Pitch}} = K_7\theta + K_8\dot{\theta} \quad (2.57)$$
$$T_{act_{Yaw}} = K_9\psi + K_{10}\dot{\psi}$$

where K_1, K_2, K_7, K_8, K_9, and K_{10} are all gains that can be selected. This allows

for the command input of roll, pitch and yaw for stabilization of those states. The

new state-space system is given by:

$$\frac{d}{dt}\begin{Bmatrix} \phi \\ \dot{\phi} \\ \theta \\ \dot{\theta} \\ \psi \\ \dot{\psi} \end{Bmatrix} = \begin{bmatrix} 0 & 1 & 0 & 0 & 0 & 0 \\ K_1 & K_2 & 0 & \dfrac{-J_B\Omega_B + J_A\Omega_A}{Ixx} & 0 & 0 \\ 0 & 0 & 0 & 1 & 0 & 0 \\ 0 & \dfrac{J_B\Omega_B + J_A\Omega_A}{Iyy} & K_7 & K_8 & 0 & 0 \\ 0 & 0 & 0 & 0 & 0 & 1 \\ 0 & 0 & 0 & 0 & K_9 & K_{10} \end{bmatrix} \begin{Bmatrix} \phi \\ \dot{\phi} \\ \theta \\ \dot{\theta} \\ \psi \\ \dot{\psi} \end{Bmatrix} \quad (2.58)$$

This gives the ability to choose values for the gains in the state-space system that

gives negative real-parts of the eigenvalues of the system making it stable.

Through a number of trials the chosen values of the gains were determined. These

gain values were chosen to be:

$$\begin{aligned} K_1 &= -175 \\ K_2 &= -58 \\ K_7 &= -175 \\ K_8 &= -58 \\ K_9 &= -1 \\ K_{10} &= -2 \end{aligned} \quad (2.59)$$

These gains resulted in the following eigenvalues for the system (c.f. Equation

(2.58)) system:

$$\lambda = \begin{Bmatrix} -55.42 + 26.34i \\ -55.42 - 26.34i \\ -2.58 + 1.22i \\ -2.58 - 1.22i \\ -1 \\ -1 \end{Bmatrix} \qquad (2.60)$$

Upon selecting the non-optimal gains by trials for the linear controller, the controller is implemented into the nonlinear rotational dynamics. In doing this, it is possible to check whether the linear controller is effective at stabilizing the nonlinear rotational dynamics. So the nonlinear rotational dynamics incorporating the linear controller is the following:

$$\ddot{\phi} = \left(\frac{1}{Ixx}\right) \cdot \left(\dot{\theta}\dot{\psi}\left(I_{yy} - I_{zz}\right) - J_B\dot{\theta}\Omega_B + J_A\dot{\theta}\Omega_A + K1\cdot\phi + K2\cdot\dot{\phi}\right)$$

$$\ddot{\theta} = \left(\frac{1}{Iyy}\right) \cdot \left(\dot{\phi}\dot{\psi}\left(I_{zz} - I_{xx}\right) + J_B\dot{\phi}\Omega_B - J_A\dot{\phi}\Omega_A + K3\cdot\theta + K4\cdot\dot{\theta}\right) \qquad (2.61)$$

$$\ddot{\psi} = \left(\frac{1}{Izz}\right) \cdot \left(\dot{\phi}\dot{\theta}\left(I_{xx} - I_{yy}\right) + K5\cdot\psi + K6\cdot\dot{\psi}\right)$$

A code was written in *MATLAB* that simulates the nonlinear rotational dynamics. So first, the nonlinear rotational dynamics were simulated with non-zero initial conditions (IC) and uncontrolled. The rotational dynamics are clearly unstable with non-zero ICs. Figure 2.4 illustrates the unstable rotational dynamics with non-zero ICs. Then, in this code the linear controller was implemented.
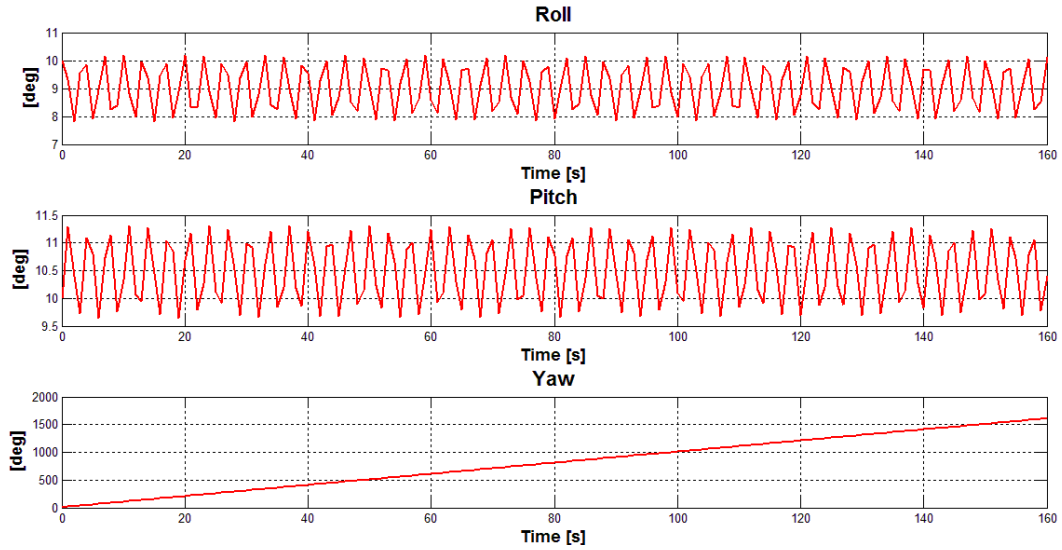
Figure 2.4. Uncontrolled nonlinear rotational dynamics with non-zero initial condition

So, the linear controller is now introduced to the nonlinear rotational dynamics with identical non-zero ICs. Figure 2.5 illustrates effect of the linear controller on the nonlinear rotational dynamics.
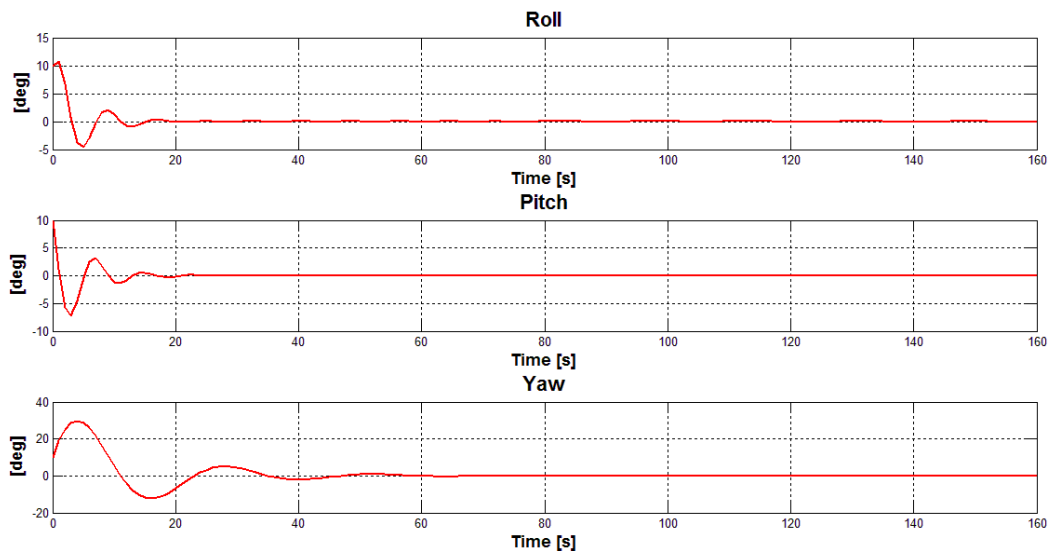

Figure 2.5. Nonlinear rotational dynamics with linear controller with non-zero ICs

25

In Figure 2.5, it can be noticed that the rotational dynamics are stabilized. The rotational dynamics are locally stabilized since a linear controller was implemented. This means that for a given domain of attraction the linear will stabilize the nonlinear rotational dynamics.

The linear controller also clearly exhibits settling time issues. The settling time is most noticeable in yaw, which approximately takes the controller 40 seconds to stabilize it. The settling time could be a cause from using insufficient gains, non-optimal gains or simply the fact that the linear controller is trying to control nonlinear rotational dynamics. In the next section an optimal linear controller will be created and implemented to the same nonlinear rotational dynamics. This will allow us to compare the performance of an optimal controller.

2.2.2 Optimal Linear Controller

An optimal linear controller will be designed comprising of the linear controller described by Equation (2.53)and utilizing the same assumptions made in Equations (2.50), (2.51), and (2.52). To design an optimal linear controller it entitles selecting the gains that would minimize the cost function:

$$J\left(\mathbf{x}(t),\mathbf{u}(t)\right) = \frac{1}{2}\cdot\mathbf{x}^T\left(tf\right)\cdot\mathbf{H}\cdot\mathbf{x}(tf) + \frac{1}{2}\int_0^{tf}\mathbf{x}^T(t)\cdot\mathbf{Q}\cdot\mathbf{x}(t) + \mathbf{R}\cdot\mathbf{u}^2(t)dt \quad (2.62)$$

where $\mathbf{H}$, $\mathbf{Q}$ and $\mathbf{R}$ are all positive semi-definite matrices of size 6x6. $\mathbf{H}$ will be assumed to be a zero matrix, while $\mathbf{Q}$ and $\mathbf{R}$ will be assumed to be identity matrices. Matrix $\mathbf{Q}$ will be multiplied by a factor of 100 indicating weight on the states. The best approach to minimize the cost function is to reduce $\mathbf{u}(t)$ which as previously mention as $\mathbf{u}(t)=\mathbf{K}(t)\mathbf{x}(t)$. One method for finding the optimal feedback

gain matrix is utilizing a nonlinear matrix differential equation, known as the

Riccati equation.

$$\dot{\mathbf{S}}(t) = -\mathbf{S}(t) \cdot \mathbf{A} - \mathbf{A}^T \cdot \mathbf{S}(t) + \mathbf{Q} + \mathbf{S}(t) \cdot \mathbf{B} \cdot \mathbf{R}^{-1} \cdot \mathbf{B}^T \cdot \mathbf{S}(t) \qquad (2.63)$$

The Riccati equation has only final conditions and can be solved backward in

time using numerical integration. The solution of an optimal control can be

reduced by finding the matrix $\mathbf{S}(t)$. The optimal gains are therefore given by:

$$\mathbf{K}(t)\mathbf{x}(t) = \mathbf{R}^{-1}\mathbf{B}^T\mathbf{S}(t)\mathbf{x}(t) \qquad (2.64)$$

Using MATLAB, a code was written to numerically integrate the Riccati

equation using ode45. The results $\mathbf{S}(t)$ were then inputted into Equation (2.64).

The results led to the population of the $\mathbf{K}$ matrix with optimal gains:

$$\mathbf{K} = \begin{bmatrix} 4.97 & 6.31 & 5.03 & -1.33 & 0 & 0 \\ 4.97 & 6.31 & 5.03 & -1.33 & 0 & 0 \\ -5.03 & -1.33 & 4.97 & 8.99 & 0 & 0 \\ -5.03 & -1.33 & 4.97 & 8.99 & 0 & 0 \\ 0 & 0 & 0 & 0 & 7.07 & 7.55 \\ 0 & 0 & 0 & 0 & 7.07 & 7.55 \end{bmatrix} \qquad (2.65)$$

Consequently the controller would be of the form $\mathbf{B} \cdot \mathbf{Kx}$ giving the following

state control inputs similar to the ones in Equation (2.53). Where the gains in

(2.54) now have the following values:

$$K_1 = -9.95$$
$$K_2 = -12.61$$
$$K_3 = -10.05$$
$$K_4 = 2.66$$
$$K_5 = 10.05$$
$$K_6 = 2.66$$
$$K_7 = -9.95$$
$$K_8 = -17.99$$
$$K_9 = -14.14$$
$$K_{10} = -15.11$$

(2.66)

These are the optimal linear gains. The optimal linear controller is then

incorporated into the nonlinear rotational dynamics as

$$\ddot{\phi} = \left(\frac{1}{Ixx}\right) \cdot \left(\dot{\theta}\dot{\psi}\left(I_{yy} - I_{zz}\right) - J_B\dot{\theta}\Omega_B + J_A\dot{\theta}\Omega_A + K1 \cdot \phi + K2 \cdot \dot{\phi} + K3 \cdot \theta + K4 \cdot \dot{\theta}\right)$$

$$\ddot{\theta} = \left(\frac{1}{Iyy}\right) \cdot \left(\dot{\phi}\dot{\psi}\left(I_{zz} - I_{xx}\right) + J_B\dot{\phi}\Omega_B - J_A\dot{\phi}\Omega_A + K1 \cdot \phi + K2 \cdot \dot{\phi} + K3 \cdot \theta + K4 \cdot \dot{\theta}\right)$$

$$\ddot{\psi} = \left(\frac{1}{Izz}\right) \cdot \left(\dot{\phi}\dot{\theta}\left(I_{xx} - I_{yy}\right) + K5 \cdot \psi + K6 \cdot \dot{\psi}\right)$$

(2.67)

In this form it is clearly evident that the controller inputs for roll and pitch are

dependent on each other to stabilize the roll and pitch. It is also evident that yaw

is independent of both roll and pitch.

A code is written in *MATLAB* that simulates the nonlinear rotational

dynamics. In this code the optimal linear controller is implemented. Figure 2.6

illustrates the optimal linear controller performing with the nonlinear rotational
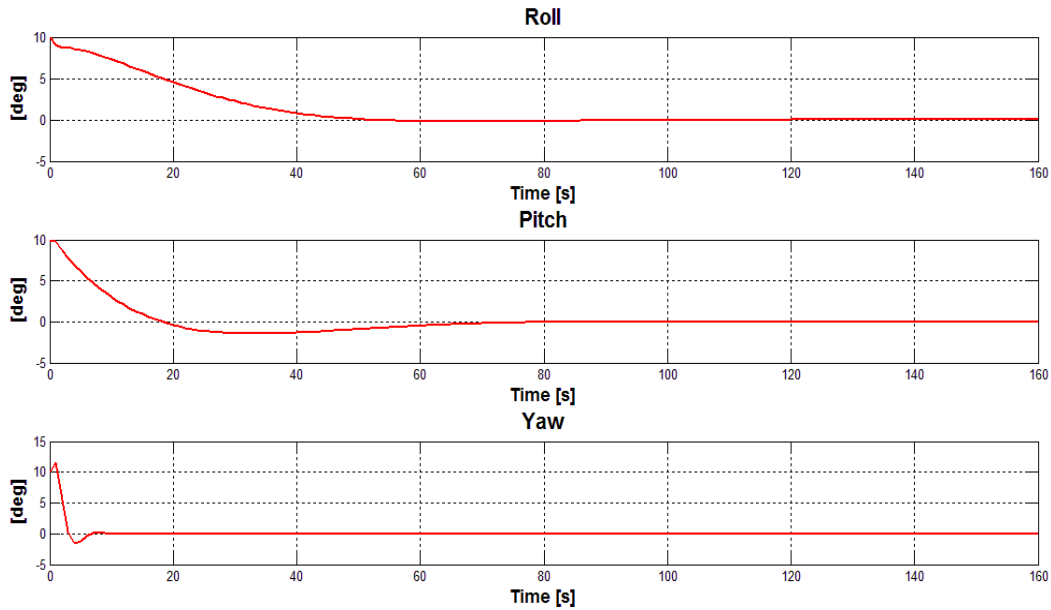
dynamics.

Figure 2.6. **Nonlinear rotational dynamics with optimal linear controller with**

non-zero ICs

The figure above shows that the states are stabilized. It is important to mention

that in similar fashion as the linear controller, the optimal linear control only

stabilizes the rotational dynamics locally. As well, from the Figure 2.6 it is

evident that the optimal controller stabilizes yaw faster than roll or pitch, as a

result that yaw is independent of roll and pitch. In roll and pitch the issue of

settling time is still very present. In the next section a nonlinear controller will be

created and implemented to the same nonlinear rotational dynamics. This will

allow us to compare the performance of the linear controller, and optimal linear

controller against the nonlinear controller.

2.2.3 Nonlinear Controller

It can be noted that the linear control may work on the nonlinear plant but

stability cannot be guaranteed. Also as the initial conditions deviate from

equilibrium solution the linear control may not work as the nonlinear effects

become predominant. In order to achieve 'global' stability a nonlinear control was proposed. The approach here would be to design the nonlinear controller using Lyapunov approach. In specifically the Lyapunov's direct method. This method is widely used in the stability analysis of general dynamical systems. It makes use of a Lyapunov function $V(\mathbf{x}, t)$. This scalar function of the state and time may be considered as some form of time dependent generalized energy. The basic idea of the method is to utilize the time rate of energy change in $V(\mathbf{x}, t)$ for a given system to judge whether the system is stable or not. The details about Lyapunov's method and stability theorems can be found in the text by Bay (1999).

For a linear system where constant coefficients are concerned, it is simple to find a Lyapunov function. Consider the linear system

$$\dot{\underset{\sim}{\mathbf{x}}}(t) = \tilde{\mathbf{A}}\underset{\sim}{\mathbf{x}}(t) \tag{2.68}$$

where $\mathbf{A}$ is a constant matrix. A quadratic form of $V(\mathbf{x})$ may be assumed as

$$V(\underset{\sim}{\mathbf{x}}) = \underset{\sim}{\mathbf{x}}^T \mathbf{P} \underset{\sim}{\mathbf{x}}$$

where $\mathbf{P}$ is a real, symmetric and positive definite matrix. Then

$$\dot{V}(\underset{\sim}{\mathbf{x}}) = \dot{\underset{\sim}{\mathbf{x}}}^T \mathbf{P}\underset{\sim}{\mathbf{x}} + \underset{\sim}{\mathbf{x}}^T \mathbf{P}\dot{\underset{\sim}{\mathbf{x}}} = (\tilde{\mathbf{A}}\underset{\sim}{\mathbf{x}})^T \mathbf{P}\underset{\sim}{\mathbf{x}} + \underset{\sim}{\mathbf{x}}^T \mathbf{P}\tilde{\mathbf{A}}\underset{\sim}{\mathbf{x}} \tag{2.69}$$

or

$$\dot{V}(\underset{\sim}{\mathbf{x}}) = \underset{\sim}{\mathbf{x}}^T (\tilde{\mathbf{A}}^T \mathbf{P} + \mathbf{P}\tilde{\mathbf{A}})\underset{\sim}{\mathbf{x}} \tag{2.70}$$

According to the Lyapunov theorem for autonomous systems, if $\dot{V}(x)$ is negative definite then the null solution is asymptotically stable (Brogan, 1974). Therefore, one can write (Bay, 1999):

$$\tilde{\mathbf{A}}^T \mathbf{P} + \mathbf{P}\tilde{\mathbf{A}} = -\mathbf{C} \tag{2.71}$$

30

where $\mathbf{C}$ is a positive definite matrix. Equation (2.71) is called the Lyapunov equation. It has been shown by Kalman and Bertram, that if $\tilde{\mathbf{A}}$ has eigenvalues with negative real parts (asymptotically stable), then for every given positive definite matrix $\mathbf{C}$, there exists a unique Lyapunov matrix $\mathbf{P}$. In this study, matrix $\mathbf{C}$ is always taken as the identity matrix. The following Lyapunov function was selected that is always positive definite.

$$V = \phi^2 + \theta^2 + \psi^2 + \dot{\phi}^2 + \dot{\theta}^2 + \dot{\psi}^2 \tag{2.72}$$

where V is Lyapunov function. The derivative of Equation (2.72) takes the following form:

$$\dot{V} = 2\dot{\phi}\ddot{\phi} + 2\phi\dot{\phi} + 2\dot{\theta}\ddot{\theta} + 2\theta\dot{\theta} + 2\dot{\psi}\ddot{\psi} + 2\psi\dot{\psi} \tag{2.73}$$

If $\dot{V}$ is negative definite, then the nonlinear rotational dynamics will be globally asymptotically stable. So the rotational dynamics for $\ddot{\phi}, \ddot{\theta}, and\ \ddot{\psi}$ are substituted into Equation (2.73) yielding.

$$
\begin{aligned}
\dot{V} &= \frac{2\dot{\phi}}{I_{xx}} \left[\dot{\theta}\dot{\psi} \left(I_{yy} - I_{zz} \right) - J_B \dot{\theta}\Omega_B + J_A \dot{\theta}\Omega_A + T_{act_{Roll}} \right] + 2\phi\dot{\phi} \\
&+ \frac{2\dot{\theta}}{I_{yy}} \left[\dot{\phi}\dot{\psi} \left(I_{zz} - I_{xx} \right) + J_B \dot{\phi}\Omega_B - J_A \dot{\phi}\Omega_A + T_{act_{Pitch}} \right] + 2\theta\dot{\theta} \quad (2.74) \\
&+ \frac{2\dot{\psi}}{I_{zz}} \left[\dot{\phi}\dot{\theta} \left(I_{xx} - I_{yy} \right) + T_{act_{Yaw}} \right] + 2\psi\dot{\psi}
\end{aligned}
$$

We assume the nonlinear controller of the form

$$
\begin{aligned}
T_{act_{Roll}} &= -K_1 \dot{\theta}\dot{\psi} - K_2 \dot{\theta} - K_3 \dot{\phi} - K_4 \phi \\
T_{act_{Pitch}} &= -K_5 \dot{\phi}\dot{\psi} - K_6 \dot{\phi} - K_7 \dot{\theta} - K_8 \theta \qquad (2.75) \\
T_{act_{Yaw}} &= -K_9 \dot{\phi}\dot{\theta} - K_{10} \dot{\psi} - K_{11} \psi
\end{aligned}
$$

31

where K_1 through K_6 are controllable gains. To determine the appropriate gains that would satisfy condition for Lyapunov stability, assumptions (2.75) were substituted into Equations (2.74). After the substitution the gains would be obtained as

$$
\begin{aligned}
K_1 &= I_{yy} - I_{zz} \\
K_2 &= -J_B \cdot \Omega_B + J_A \cdot \Omega_A \\
K_3 &= a \cdot I_{xx} \\
K_4 &= I_{xx} \\
K_5 &= I_{zz} - I_{xx} \\
K_6 &= J_B \cdot \Omega_B - J_A \cdot \Omega_A \\
K_7 &= a \cdot I_{yy} \\
K_8 &= I_{yy} \\
K_9 &= I_{xx} - I_{yy} \\
K_{10} &= a \cdot I_{zz} \\
K_{11} &= I_{zz}
\end{aligned}
\tag{2.76}
$$

where a is any number that is less than zero. By implementing these gains Equation (2.74) is reduced to:

$$
\dot{V} = -2a\dot{\phi}^2 - 2a\dot{\theta}^2 - 2a\dot{\psi}^2
\tag{2.77}
$$

Thus, Equation (2.77) will be always negative definite satisfying the condition for Lyapunov stability.

The nonlinear controller along with the gains were implemented into the nonlinear rotational dynamics. Equation (2.78) illustrates the rotational dynamics with the nonlinear controller.

$$\ddot{\phi} = \left(\frac{1}{Ixx}\right) \cdot \left(\dot{\theta}\dot{\psi}\left(I_{yy} - I_{zz}\right) - J_B\dot{\theta}\Omega_B + J_A\dot{\theta}\Omega_A - \left(I_{yy} - I_{zz}\right)\dot{\theta}\dot{\psi} - \left(-J_B \cdot \Omega_B + J_A \cdot \Omega_A\right)\dot{\theta} - aI_{xx}\dot{\phi} - I_{xx}\phi\right)$$

$$\ddot{\theta} = \left(\frac{1}{Iyy}\right) \cdot \left(\dot{\phi}\dot{\psi}\left(I_{zz} - I_{xx}\right) + J_B\dot{\phi}\Omega_B - J_A\dot{\phi}\Omega_A - \left(I_{zz} - I_{xx}\right)\dot{\phi}\dot{\psi} - \left(J_B \cdot \Omega_B - J_A \cdot \Omega_A\right)\dot{\phi} - aI_{yy}\dot{\theta} - I_{yy}\theta\right)$$

$$\ddot{\psi} = \left(\frac{1}{Izz}\right) \cdot \left(\dot{\phi}\dot{\theta}\left(I_{xx} - I_{yy}\right) - \left(I_{xx} - I_{yy}\right)\dot{\phi}\dot{\theta} - aI_{zz}\dot{\psi} - I_{zz}\psi\right)$$

$$(2.78)$$

A code is written in *MATLAB* that simulates the nonlinear rotational

dynamics. In this code the nonlinear controller is implemented. Figure 2.7

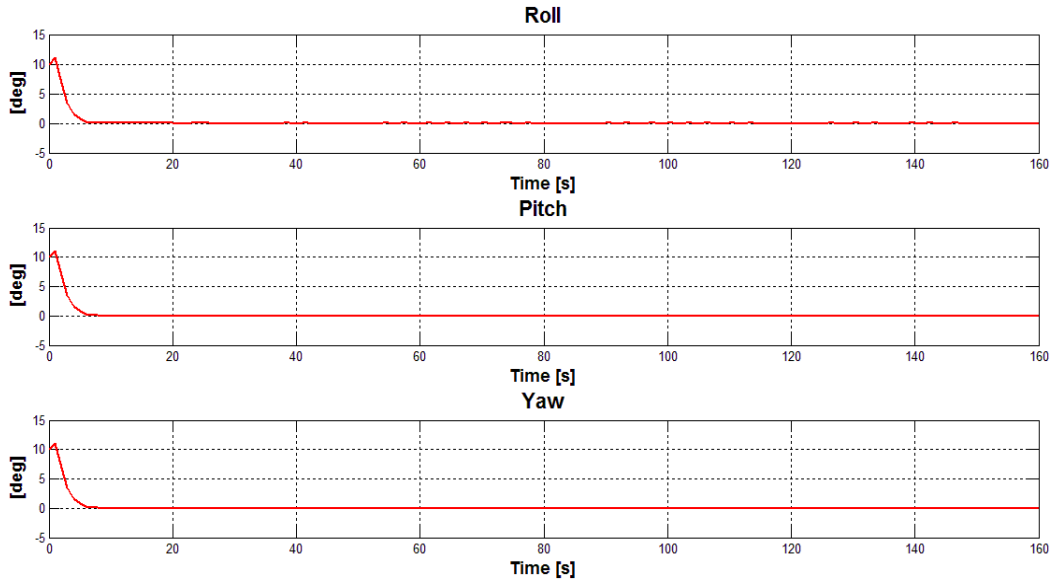demonstrates the nonlinear controller at work with non-zero ICs for the rotational

dynamics.

Figure 2.7. **Rotational dynamics with nonlinear controller with non-zero ICs**

It is evident that nonlinear controller stabilizes the rotational dynamics. It is

important to note that the nonlinear controller not only stabilized the rotational

dynamics but in addition made the rotational dynamics globally stable. This

means the rotational dynamics will always be stable no matter if large ICs are

provided. As well, the nonlinear controller exhibits some settling time. Though,

this settling time of the nonlinear controller is much smaller than that of the linear

controller or optimal linear controller. Figure 2.8 illustrates a comparison between

the linear controller, optimal linear controller and the nonlinear controller at

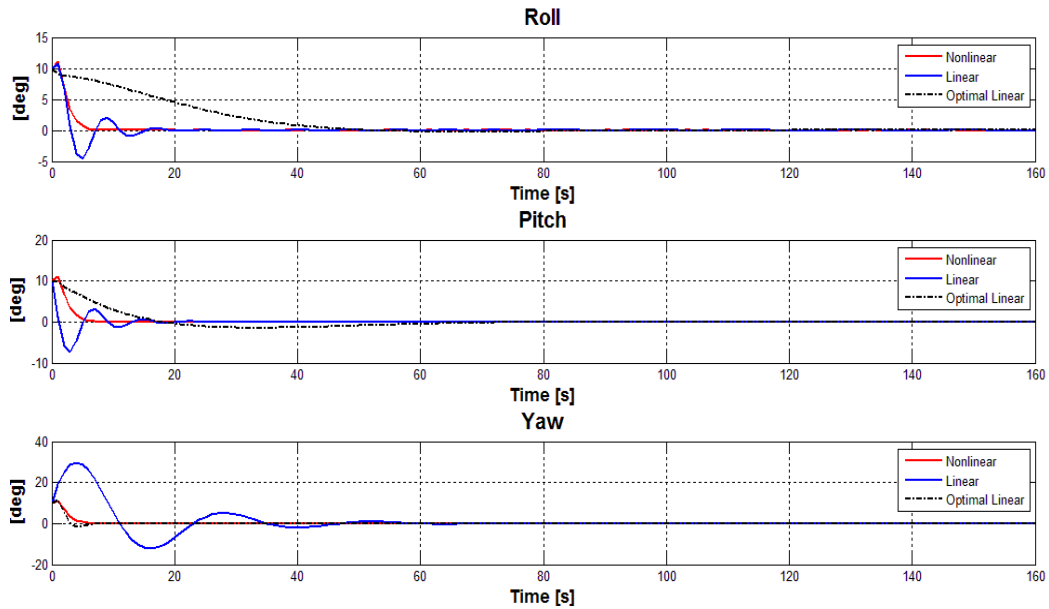stabilizing the same rotational dynamics with identical non-zero ICs.

Figure 2.8. **Comparison between nonlinear versus linear versus optimal**

linear controllers

From the Figure 2.8 it is evident that the nonlinear controller has a quicker

response at stabilizing the rotational dynamics. From Figure 2.8, one can conclude

that the nonlinear controller is better performing than the both linear and optimal

linear controllers. The controller effort was also calculated for the linear, optimal

linear and nonlinear controllers. This allows for a more complete assessment of

the performance of all controllers. Figure 2.9 demonstrates the controller effort

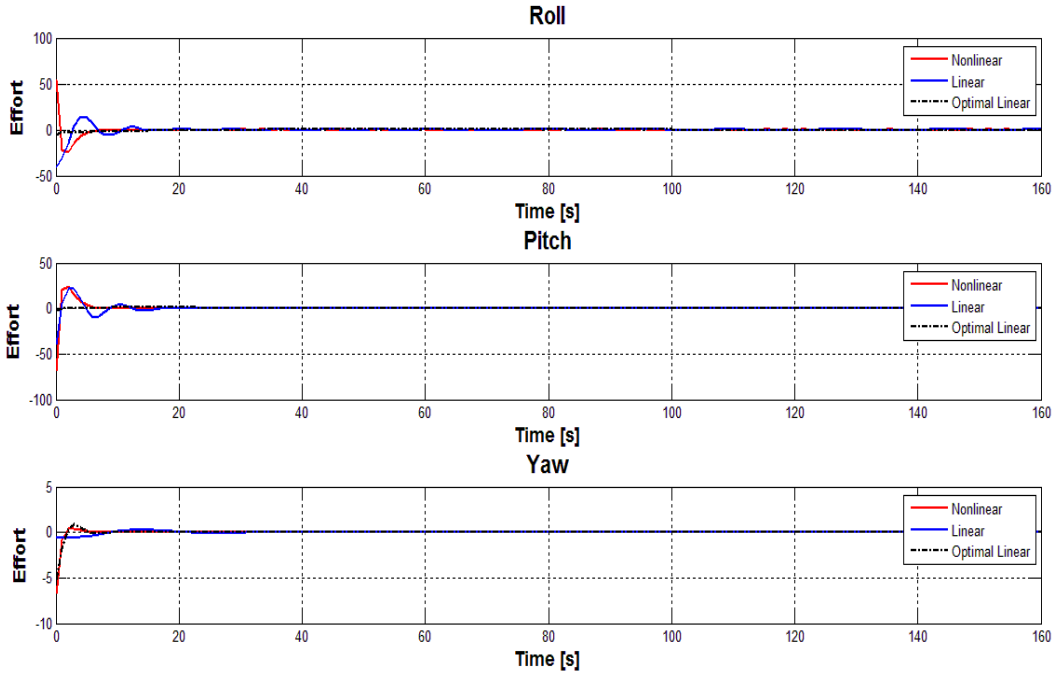for the nonlinear, linear controller and optimal linear controller.

Figure 2.9. **Nonlinear, linear, and optimal linear controller effort**

Initially the effort for the nonlinear controller at stabilizing the three states (roll,

pitch, and yaw) is more than that of the linear and optimal linear controller. As

well, the nonlinear controller demonstrates the most effort at the beginning as

oppose to the linear and optimal linear controller. The linear controller

demonstrates controller effort throughout a larger range of time, while the optimal

linear controller demonstrates the least controller effort.

2.3   Robustness

In this section, we briefly remark on the robustness analysis of the controller. It

can be observed that an exact plant dynamics is difficult to model due to

uncertainties in modeling. A controller that functions adequately for all

admissible perturbations is termed robust (Burl, 1999). Generally the uncertainty

is classified as unstructured uncertainty where the uncertainty is modeled by

connecting unknown but bounded perturbations to the plant or structured

35

uncertainty where additional constraints on the uncertainty are available. These constraints provide structure to the set of admissible perturbations (Burl, 1999). In the example of Stop-Rotor UAV the structured uncertainty could be nominal weight or inertia properties plus a perturbation (payload variation).

Consider the linearized plant dynamics given by Equation (2.49) with the controller, the 'stabilized' plant dynamics is given by

$$\dot{\mathbf{x}} = (\mathbf{A} + \mathbf{B}\mathbf{K})\mathbf{x} \tag{2.79}$$

It is noted that previously we assumed that the inertia properties remain unchanged. Now assume that the inertia properties change with known bounds. The Equation (2.79) can be written as

$$\dot{\mathbf{x}} = (\mathbf{A} + \mathbf{G}(t) + \mathbf{B}\mathbf{K})\mathbf{x} \tag{2.80}$$

where $\mathbf{G}(t)$ is the time varying perturbation. Equation (2.80) can be written as

$$\dot{\mathbf{x}} = [\bar{\mathbf{A}} + \mathbf{G}(t)]\dot{\mathbf{x}} \tag{2.81}$$

where $\bar{\mathbf{A}} = \mathbf{A} + \mathbf{B}\mathbf{K}$

It is to be noted that $\bar{\mathbf{A}}$ is a constant matrix whose eigenvalues have negative real parts. We follow the approach presented by Infante (1969) to obtain stability bounds.

Theorem: If, for some positive definite matrix $\tilde{\mathbf{B}}$ and some $\varepsilon > 0$,

$$E\{\lambda_{\max}[(\bar{\mathbf{A}} + \mathbf{G}(t))^T + \tilde{\mathbf{B}}(\bar{\mathbf{A}} + \mathbf{G}(t))\tilde{\mathbf{B}}^{-1}]\} \leq -\varepsilon \tag{2.82}$$

then Equation (2.81) is almost surely asymptotically stable in the large, where $E\{\}$ is the expectation operator, and $\lambda_{\max}$ is maximum real eigenvalue.

Proof: Consider the quadratic (Lyapunov) function $V(\mathbf{x}) = \mathbf{x}^T \tilde{\mathbf{B}} \mathbf{x}$ as before.

Then along the trajectories of Equation (2.81), define

$$\lambda(t) = \frac{\dot{V}(\mathbf{x})}{V(\mathbf{x})} = \frac{\mathbf{x}^T [(\bar{\mathbf{A}} + \mathbf{G}(t))^T \tilde{\mathbf{B}} + \tilde{\mathbf{B}}(\bar{\mathbf{A}} + \mathbf{G}(t))]\mathbf{x}}{\mathbf{x}^T \tilde{\mathbf{B}} \mathbf{x}} \qquad (2.83)$$

It is noted that the numerator and denominator in Equation (2.83) are quadratic

forms. The pencil of quadratic forms $\hat{\mathbf{A}}(\mathbf{x}, \mathbf{x}) = \sum_{i,k=1}^{n} a_{ik} x_i x_k$ and $\hat{\mathbf{B}}(\mathbf{x}, \mathbf{x}) = \sum_{i,k=1}^{n} b_{ik} x_i x_k$

a matrix valued function defined over complex numbers λ given by

$\hat{\mathbf{A}}(\mathbf{x}, \mathbf{x}) + \lambda \hat{\mathbf{B}}(\mathbf{x}, \mathbf{x})$ (Gantmacher, 1977). For the details and the properties on the

pencils of quadratic forms and matrices, we refer to the references (Bai et al.,

2000).

Define $\|\mathbf{x}\|_p = \left(\mathbf{x}^T \tilde{\mathbf{B}} \mathbf{x}\right)^{1/2}$. It can be shown (Kozin, 2000) that $\|\mathbf{x}\|_p$ satisfies

$$\frac{d}{dt} \log \|\mathbf{x}\|_p = \frac{\mathbf{x}^T [(\bar{\mathbf{A}} + \mathbf{G}(t))^T \tilde{\mathbf{B}} + \tilde{\mathbf{B}}(\bar{\mathbf{A}} + \mathbf{G}(t))]\mathbf{x}}{\mathbf{x}^T \tilde{\mathbf{B}} \mathbf{x}} \qquad (2.84)$$

integrating and dividing Equation (2.84) by t,

$$\frac{1}{t}[\log \|\mathbf{x}(t)\|_p - \log \|\mathbf{x}(0)\|_p] = \frac{1}{t} \int_0^t \frac{\mathbf{x}^T [(\bar{\mathbf{A}} + \mathbf{G}(s))^T \tilde{\mathbf{B}} + \tilde{\mathbf{B}}(\bar{\mathbf{A}} + \mathbf{G}(s))]\mathbf{x}}{\mathbf{x}^T \tilde{\mathbf{B}} \mathbf{x}} ds \qquad (2.85)$$

For $\frac{1}{t}[\log \|\mathbf{x}(t)\|_p - \log \|\mathbf{x}(0)\|_p] < 0$ as $t \to \infty$ it must follow that $\lim_{t \to \infty} \|\mathbf{x}(t)\| = 0$.

Thus, the algebraic sign of $\lim_{t \to \infty}[\frac{1}{t} \int_0^t \frac{\mathbf{x}^T [(\bar{\mathbf{A}} + \mathbf{G}(s))^T \tilde{\mathbf{B}} + \tilde{\mathbf{B}}(\bar{\mathbf{A}} + \mathbf{G}(s))]\mathbf{x}}{\mathbf{x}^T \tilde{\mathbf{B}} \mathbf{x}} ds]$ provides

the condition for the stability (Kozin, 2000). It is noted that if $\mathbf{G}(t)$ is assumed

stochastic then ergodicity would be required if we want to evaluate

$$\lim_{t \to \infty}[\frac{1}{t}\int_0^t \frac{\mathbf{x}^T[(\bar{\mathbf{A}}+\mathbf{G}(s))^T\tilde{\mathbf{B}}+\tilde{\mathbf{B}}(\bar{\mathbf{A}}+\mathbf{G}(s))]\mathbf{x}}{\mathbf{x}^T\tilde{\mathbf{B}}\mathbf{x}}ds]$$ using expectation operator $E\{\}$

(Kozin, 2000).

From the properties of pencils of quadratic forms (Gantmacher, 1977), the

quotient $\dfrac{\mathbf{x}^T[(\bar{\mathbf{A}}+\mathbf{G}(t))^T\tilde{\mathbf{B}}+\tilde{\mathbf{B}}(\bar{\mathbf{A}}+\mathbf{G}(t))]\mathbf{x}}{\mathbf{x}^T\tilde{\mathbf{B}}\mathbf{x}}$ (c.f. Equation (2.84)) satisfies

$$\lambda_{min}\{[(\bar{\mathbf{A}}+\mathbf{G}(t))^T\tilde{\mathbf{B}}+\tilde{\mathbf{B}}(\bar{\mathbf{A}}+\mathbf{G}(t))]\tilde{\mathbf{B}}^{-1}\} \leq \lambda(t) \leq \lambda_{max}\{[(\bar{\mathbf{A}}+\mathbf{G}(t))^T\tilde{\mathbf{B}}+\tilde{\mathbf{B}}(\bar{\mathbf{A}}+\mathbf{G}(t))]\tilde{\mathbf{B}}^{-1}\}$$
(2.86)

where λ_{max} is defined before and λ_{min} is the minimum real eigenvalues of the

matrix pencil $[(\bar{\mathbf{A}}+\mathbf{G}(s))^T\tilde{\mathbf{B}}+\tilde{\mathbf{B}}(\bar{\mathbf{A}}+\mathbf{G}(s))]\tilde{\mathbf{B}}^{-1}$. After expansion, Equation (2.86)

can be written as

$$\lambda_{min}\{(\bar{\mathbf{A}}+\mathbf{G}(t))^T+\tilde{\mathbf{B}}(\bar{\mathbf{A}}+\mathbf{G}(t))\tilde{\mathbf{B}}^{-1}\} \leq \lambda(t) \leq \lambda_{max}\{[(\bar{\mathbf{A}}+\mathbf{G}(t))^T+\tilde{\mathbf{B}}(\bar{\mathbf{A}}+\mathbf{G}(t))\tilde{\mathbf{B}}^{-1}\}$$

(2.87)

Thus, the solution of Equation (2.83) can be given as

$$V[\mathbf{x}(t)] = V[\mathbf{x}(t_0)]e^{\int_{t_0}^t \lambda(\tau)d\tau} \equiv V[\mathbf{x}(t_0)]e^{(t-t_0)[\frac{1}{t-t_0}\int_{t_0}^t \lambda(\tau)d\tau]}$$
(2.88)

It can be observed that, if $E\{\lambda(t)\} \leq -\varepsilon$ for some $\varepsilon > 0$, $V[\mathbf{x}(t)]$ is bounded and

that $V[\mathbf{x}(t)] \to 0$ as $t \to \infty$.

Thus, we can observe that as long as the condition given by theorem is

satisfied the linear controller will stabilize the UAV in presence of perturbation.

Chapter 3

EXPERIMENTAL VALIDATION TEST AND TRANSITION MODEL

In order to demonstrate the conversion between rotary aircraft mode to fixed-wing aircraft mode, an experimental validation test was performed. The objective of this test drop was to prove the concept that the Stop-Rotor UAV has the ability to transition between rotary aircraft mode to fixed-wing aircraft mode and vice versa. As well as to test the collective (feathering) mechanism and to gather crucial data via Ardupilot's data logging capability. This chapter consists of two major sections. The first section will focus on the experimental validation test and all other worked related to the drop test. The second section of this chapter will focus on developing a mathematical model that will be used to analyze the transition flight of the aircraft.

3.1 Experimental Validation Test

In this drop test an unpowered Stop-Rotor UAV test specimen was dropped from a hot air balloon with the wings and tail fins pitched for rotary aircraft mode (for autorotation), then the collective (feather) mechanism was engaged to transition to fixed-wing mode position for the wings and tail fins, then the fixed-wing aircraft was pulled out of the dive and allowed glide before pushing over and pitching the wings and tail fins back into their previous rotary aircraft mode position and land as shown in Figure 3.1.
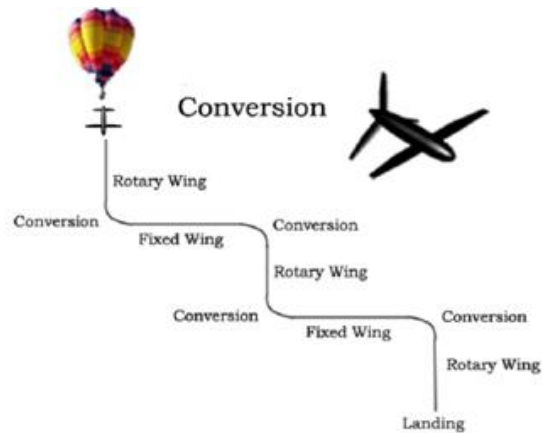
Figure 3.1. **Stop-Rotor UAV 'Big Drop' test**

During the drop test an Ardupilot (a COTS autopilot) was used for data

logging with the addition of an on board video recording of the test. All of the

data that was gathered was used to further validate the aircraft transition. A simple

mathematical model for computation of rotor speed in rotary aircraft mode was

used (Drier, 2007) and was compared to the experimental results.

3.1.1 Collective Feathering Mechanism and Ardupilot

Collective feathering of the wing is the most important aspect of this design

which enables the aircraft to transition from rotary wing to fixed-wing

configuration and vice versa. The wing collective control is obtained by 2

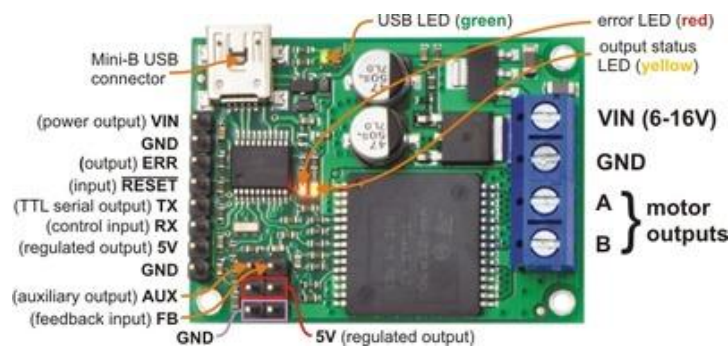independent motor controllers shown in Figure 3.2.

Figure 3.2. **Motor controller for wing control**

Each controller is powered by a separate battery pack. An RC interface is provided for collective and flaps control. Following fail safe mechanism were incorporated in the wing collective control.

a. Electronic overrun stop

b. Mechanical overrun stop

c. Current limiting control

These electro-mechanical controls would ensure that the Stop-Rotor UAV will not lose control and wings would return to trim conditions in case of an overrun.

In order to log the data from the drop test, an open source autopilot, Ardupilot was used (Anderson, 2010). This instrumentation comprises of an autopilot that has static and pitot pressure sensor, thermopiles and global positioning system (GPS). This autopilot was used in data logging mode along with zigbee wireless transmitter and receiver, and a ground station as shown in Figure 3.3. It is anticipated that this instrumentation will be used as an autopilot for Stop-Rotor to make it an unmanned aerial vehicle.

Figure 3.3. **Ardupilot (Anderson, 2010) components and interface for Stop-Rotor UAV**

The ground station interface was implemented using another open source software

(Anderson, 2010) however, the LabVIEW interface was modified to incorporate

data logging capability as shown in Figure 3.4. This ground station interface

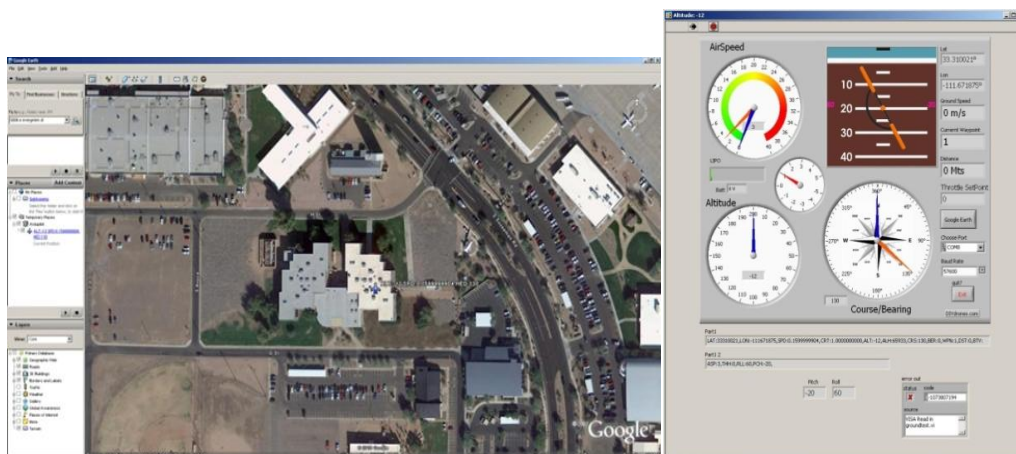shows airspeed, GPS location, attitude and altitude of the aircraft.

Figure 3.4. **LabVIEW ground station interface**

Though for the drop test only airspeed, inertial measurement unit (IMU) and GPS data were recorded.

3.1.2 Experimental and Mathematical Rotor Speed Results Comparison

In this section a comparison of the experimental validation results of the rotor speed data and the results of the mathematical model will be analyzed.

First, the rotor speed during the experimental drop test was obtained by analyzing the video recording of the drop. The rotor RPM was obtained by measuring the number of revolutions per each video time stamp. These results were then plotted versus time and are illustrated in Figure 3.5.

Second, a simple mathematical model was used to simulate the rotor speed. It is noted that the drop test is unpowered the expression for rotor speed in autorotation can be directly used to compute rotor RPM and velocity. These expression and their derivations are given in reference (Drier, 2007). Thus, following the development from reference (Drier, 2007), we assume the first order equation for rotor speed

$$\mathbf{J}\dot{\Omega} = \mathbf{Q}_{eng} - \mathbf{Q}_{rotor} \tag{3.1}$$

Where $\mathbf{J}$ is the inertia, $\dot{\Omega}$ is the angular velocity, $\mathbf{Q}_{eng}, \mathbf{Q}_{rotor}$ are the engine torque and the rotor torque, respectively. The rotor torque $\mathbf{Q}_{rotor}$ and thrust $\mathbf{T}$ can be modeled as:

$$\mathbf{Q}_{rotor} = \left(\frac{\Omega}{\Omega_0}\right)^2 \mathbf{Q}_0 \tag{3.2}$$

$$\mathbf{T} = \left(\frac{\Omega}{\Omega_0}\right)^2 \mathbf{W} \tag{3.3}$$

Where Ω_0 is the initial speed and $\mathbf{W}$ is the weight. During the unpowered test drop, engine torque, $\mathbf{Q}_{eng} = 0$ and the rotor speed equation is given by:

$$\mathbf{J}\dot{\Omega} = -\left(\frac{\Omega}{\Omega_0}\right)^2 \mathbf{Q}_0$$

(3.4)

This is called Bernoulli's equation with the closed form solution

$$\Omega(t) = \frac{\Omega_0}{1 + \dfrac{\mathbf{Q}_0 t}{\mathbf{J}\Omega_0}}$$

(3.5)

The equation of vertical motion during the test drop (i.e. free fall) is given by

$$\ddot{y} = g(1 - \frac{\mathbf{T}}{\mathbf{W}}) = g[1 - \left(\frac{\Omega}{\Omega_0}\right)^2]$$

(3.6)

Equation (3.5) is substituted in Equation (3.6) and integrated numerically once for velocity $\dot{y}$ and twice for position y determination. The simulation results were obtained by numerically integrating dynamical equations of motion. Then, the simulation results were compared to the experimental results, which are shown in Figure 3.5. It is noted that initially from time t=2 seconds results, when the Stop-Rotor UAV is in autorotation mode results are comparable. However, the difference between Expt. RPM and simulation RPM increases as time increases. The difference between simulation and experimental results can be attributed to approximate aerodynamic modeling, approximate mathematical model for the Stop-Rotor UAV and numerical integration error.
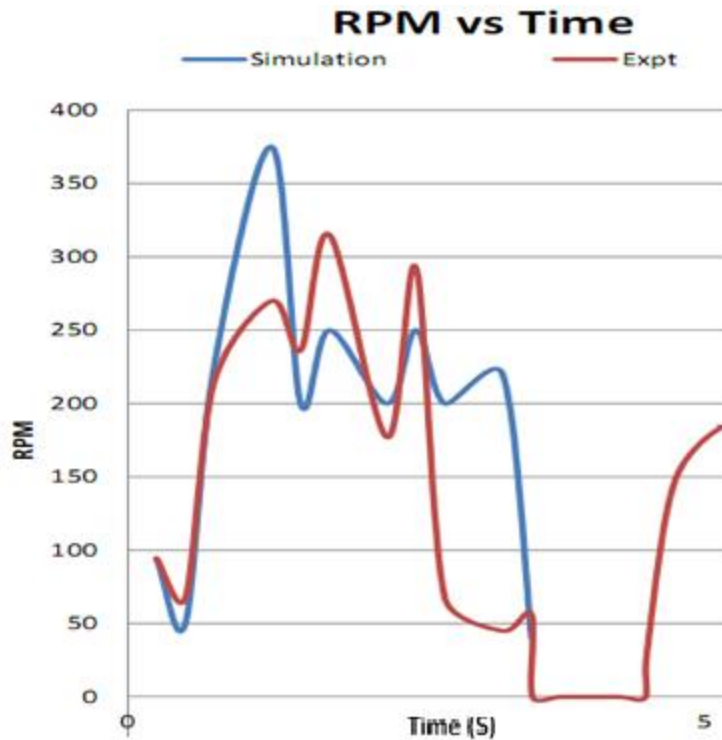
Figure 3.5. **Comparison of simulation and experimental results**

3.2   Transition Mathematical Model

For transition from helicopter mode to airplane mode and vice versa, the tail

rotor stops and helicopter in a dive, control surfaces on the wings pull the

aircraft out of dive and glide, pusher propeller is powered on and provides the

thrust required. In the airplane mode, the design resembles a flying wing airplane.

The transition will be performed in the direction of heading in the airplane

mode, hence we derive 2-D equations for transition as reference in (Osborne,

2007). Consider the aircraft transitioning from a helicopter mode to airplane mode

as shown in Figure 3.6. L and D represent the lift and drag T indicates thrust, α

and θ indicates angle of attack and pitch angle, respectively, V is the forward
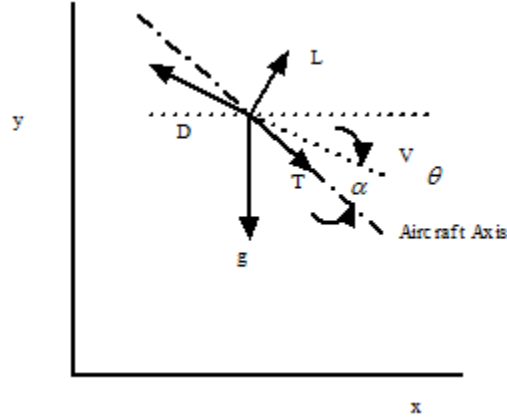
velocity.

45

Figure 3.6. **Free body diagram of Stop-Rotor**

Equations of motion can be written as:

$$m\begin{pmatrix} \ddot{x} \\ \ddot{y} \end{pmatrix} = \mathbf{G} + \mathbf{L} + \mathbf{D} + \mathbf{T}$$

$$\dot{\theta} = k(\theta_c - \theta)$$

(3.7)

Where θ_c, is the commanded pitch angle and k is the gain. In the inertial frame

the gravity vector is given as $\mathbf{G} = \begin{pmatrix} 0 \\ -mg \end{pmatrix}$

Assuming that the thrust T is along the axis of the aircraft $\mathbf{T} = \mathbf{R}(\theta)\begin{pmatrix} T \\ 0 \end{pmatrix}$ where

$\mathbf{R}(\theta)$ the rotational matrix from body coordinates to inertial coordinates. The lift

and drag vectors are given as

$$\mathbf{L} = \mathbf{R}(\theta - \alpha)\begin{bmatrix} 0 \\ L \end{bmatrix}$$

$$\mathbf{D} = \mathbf{R}(\theta - \alpha)\begin{bmatrix} -D \\ 0 \end{bmatrix}$$

(3.8)

Airspeed is given by $V = \sqrt{\dot{x}^2 + \dot{y}^2}$ and angle of attack is given by $\alpha = \theta - \tan^{-1}\begin{bmatrix} \dot{y} \\ \dot{x} \end{bmatrix}$.

46

It can be noted that transition control problem can be viewed as a trajectory tracking where the Stop-Rotor UAV transitions from a controlled hover to fixed-wing flight and vice versa
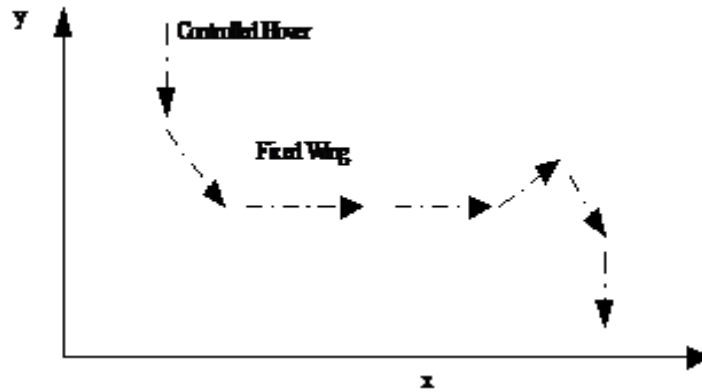

Figure 3.7. **Overview of the transition from hover to horizontal flight**

The trajectory tracking algorithm will generate values of $x, \dot{x}, \ddot{x}, y, \dot{y}, \ddot{y}$. The input to algorithm will be time t_f to perform transition and final speed V_f. The pitch

control values can be computed as $\theta = \alpha + \tan^{-1}\left[\dfrac{\dot{y}}{\sqrt{\dot{x}^2 + \dot{y}^2}}\right]$. There are multiple

methods to develop this trajectory algorithm some of them include a Lyapunov based controller, feedback linearization and model predictive adaptive control.

Chapter 4

FIXED-WING AIRCRAFT PERFORMANCE

As previously mentioned, the Stop-Rotor UAV has the capability of fixed-wing flight. It is important that performance of this aircraft in this flight mode be analyzed and evaluated. Therefore, one of the objectives of this research was to analyze the performance of the existing Stop-Rotor UAV in fixed-wing aircraft mode. This chapter is split into two sections. First section will focus on the performance analysis of the whole aircraft, and the second section will focus on the performance analysis of the main wing structure that is later used to perform stress analysis on the wings. Both performance analyses will be conducted while the aircraft is in fixed-wing flight. As well, it is important to note that in both analyses XLFR5 software is used. XFLR5 is a software package that allows the analysis of airfoils, wings and airplanes operating at a low Reynolds number (XFLR5, 2010).

4.1 Aircraft Performance

The first step for setting up the analysis of the whole aircraft was to first create the airplane geometry using XFLR5 software. The body, which is the fuselage, was first constructed; it was created by using circular cross-sections with varying radii where the smaller radii are located at the front and rear ends of the aircraft. Figure 4.1 illustrates the body of the aircraft using XFLR5.
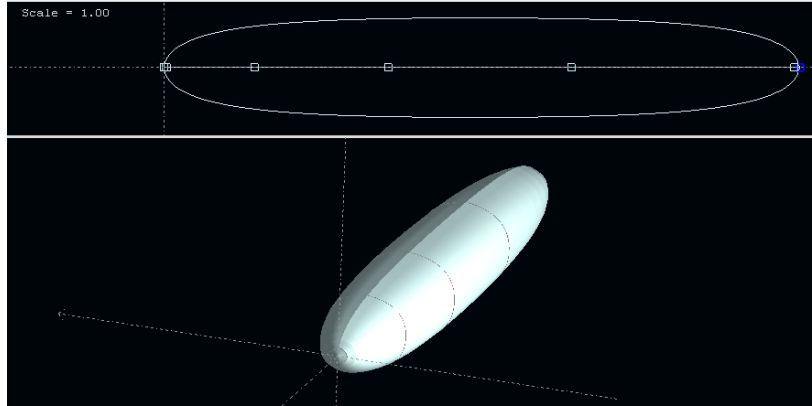
Figure 4.1 **Side view (Top) and 3-D body (Bottom) of aircraft geometry**

After creating the body, the wings, elevators and fin of the aircraft were created

by defining the chord length, span and airfoil. The airfoil for the wings, elevators

and fin were all selected to be NACA 0012. For the elevators a -30° dihedral

angel was set. The locations of the wings, elevators and fin relative to the body

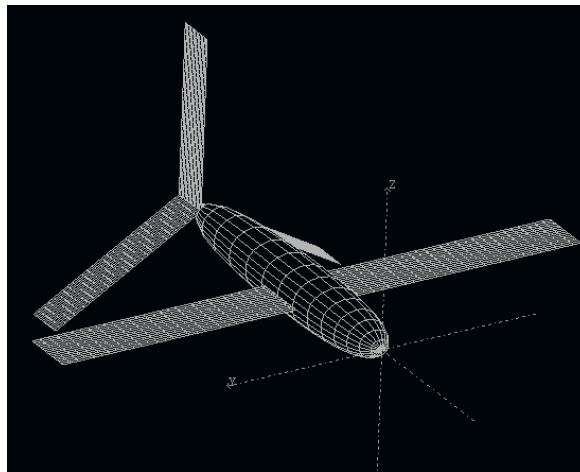were then defined. The complete fixed-wing aircraft geometry is illustrated in

Figure 4.2.

Figure 4.2. **Complete fixed-wing aircraft meshed geometry**

Upon completing the airplane geometry, an analysis on the NACA 0012

airfoil was conducted. This was done by creating a list of Reynolds number in

which the airfoil coefficients of lift, drag and moment were obtained at various

angles of attack. This airfoil analysis would supply the fixed-wing aircraft analysis with the flight envelope of the analysis as discussed in reference (Deporris, 2010).

Lastly, the fixed-wing aircraft performance was analyzed. To begin the analysis following flight and airplane characteristics were established:

Free Stream Speed = 31.29 m/s

Polar Type = Fixed Speed

X COG = 18 inches

where, X COG refers to the x-coordinate of the center of gravity (COG) of the aircraft. The location of COG was initially automatically calculated from the masses of the body, wings, elevators and fins. But it was moved on purpose to 18 inches to simulate the counter weight that was added on the specimen during the experimental validation "Big Drop" test. This was done to make the Stop-Rotor UAV specimen nose heavy during the test. The next step was to select a sequence of angle of attacks (AoA) in which the aircraft would be analyzed. The range was selected to be from -5° to 16°. The analysis was finally conducted using XFLR5.

The results of the analysis are the stall angle of the aircraft, the stability of the aircraft, and key parameters such as coefficient of lift, drag, and moment at various angles of attack.

The stall angle was determined from the analysis to be around 15°. This was determined by results of the analysis, when XFLR5 was unable to interpolate the coefficient of lift at that particular AoA, hinting that it had reached the stall

angle, even though the Reynolds number was within the flight envelope's domain.

Figure 4.3 illustrates the XFLR5 results of the aircraft analysis at the stall angle.

```
Computing Plane for alpha=  15.00°
  Calculating aerodynamic coefficients...
    Calculating wing...STOP_ROTOR PLANE_Wing
      Span pos =    -32.55 in,  Re =   556 336,  Cl =   1.26 could not be interpolated
      Span pos =    -30.93 in,  Re =   556 336,  Cl =   1.27 could not be interpolated
      Span pos =    -29.32 in,  Re =   556 336,  Cl =   1.28 could not be interpolated
      Span pos =    -27.70 in,  Re =   556 336,  Cl =   1.29 could not be interpolated
```

Figure 4.3. **Results from XFLR5 not been able to interpolate at stall angle**

This was further reinforced when the plot of coefficient of lift for airfoil was

analyzed at Reynolds number that are near, or at that value. The coefficient of lift

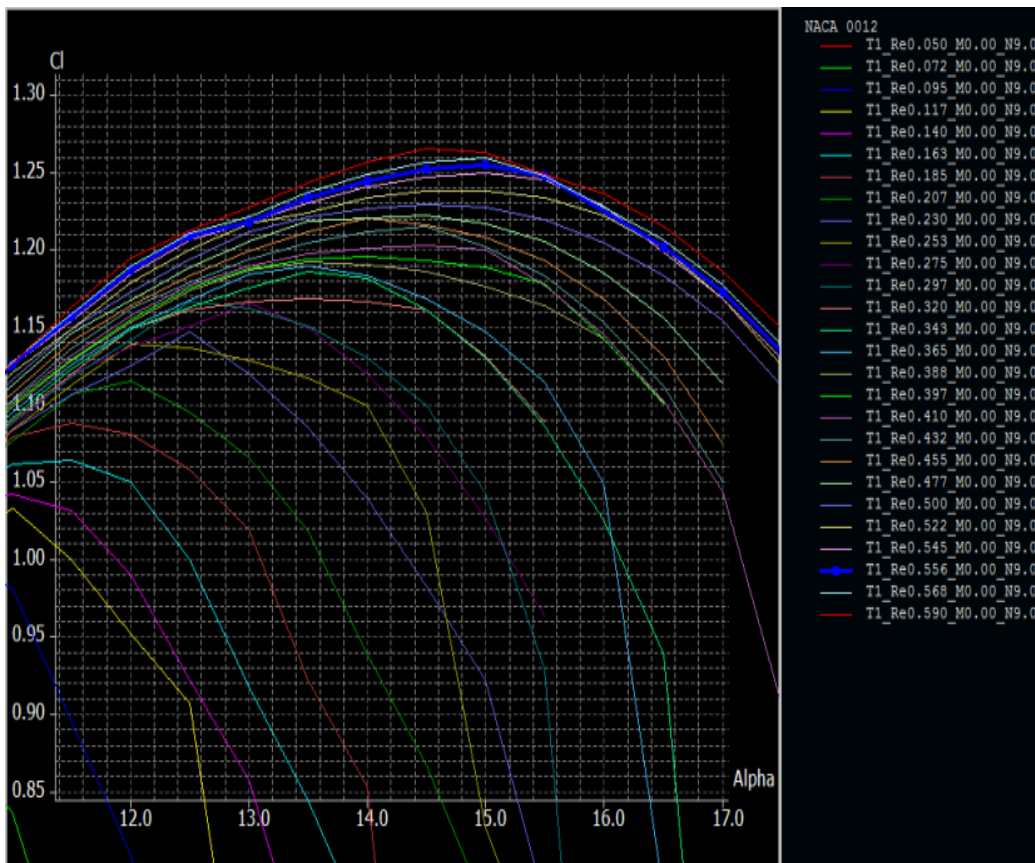of 1.26 is unachievable at Reynolds number 556,336 as shown in Figure 4.4.

Figure 4.4. **Plot of coefficient of lift for airfoil NACA 0012 at various Reynolds number**

It is also important to note that the stall angle for this airfoil at Reynolds number

of 556,336 is at approximately an AoA of 15° as in determined in reference (Anderson, 1999).

The next aircraft performance obtained from XFLR5 was the stability of the aircraft. As mention in the reference from Meschia (2008) stability in this context is the inclination for the aircraft to keep its pitch manner against any disturbances that it might encounter as found in reference (Meschia, 2008). The stability of the aircraft was determined by analyzing the polar plot of the pitching moment coefficient (Cm) versus the AoA. Figure 4.5 illustrates this plot.
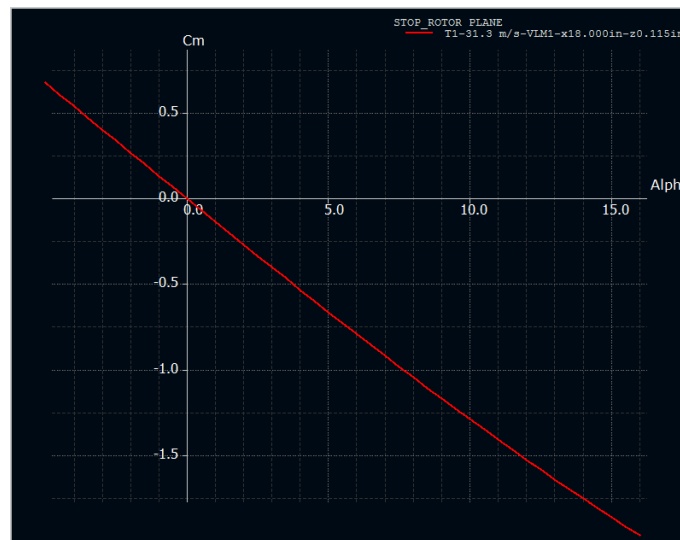

Figure 4.5. **Aircraft's plot of Cm versus AoA**

The slope of this curve is clearly negative for a range of AoA of -5° to 16°. This plot indicates that the design of the fixed-wing aircraft is stable for all of the AoA in that range. The physical meaning is that the aircraft flies balance at approximately an AoA of -0.016°.
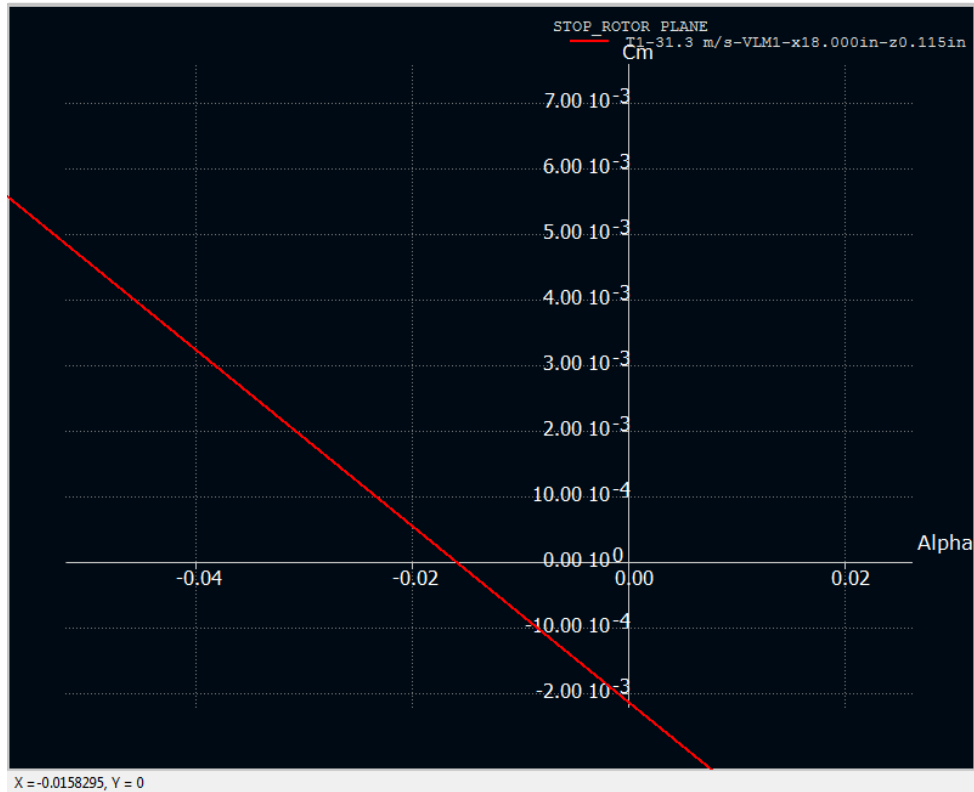
STOP_ROTOR PLANE
T1-31.3 m/s-VLM1-x18.000in-z0.115in
Cm

7.00 10^{-3}
6.00 10^{-3}
5.00 10^{-3}
4.00 10^{-3}
3.00 10^{-3}
2.00 10^{-3}
10.00 10^{-4}
0.00 10^{0}
Alpha
-0.04   -0.02   0.00   0.02
-10.00 10^{-4}
-2.00 10^{-3}

X = -0.0158295, Y = 0

Figure 4.6. **Plot of Cm vs. AoA focusing on point (-0.0158°, 0)**

As well, the graph implies that if the aircraft were to encounter a disturbance, eg. a wind gust, that makes the aircraft to take an AoA of attack, such as zero degrees. Figure 4.6 illustrates that the plot at zero degrees AoA the aircraft develops a negative pitching moment coefficient which is a nose-down moment that pushes the aircraft to its original AoA, and therefore the aircraft is longitudinally stable.

The wing structure performance is of great importance, as this component is essential to the aircraft's performance in fixed-wing flight. Before the experimental drop test was performed, a wing structural performance was conducted. In following section the aerodynamic loads experienced by the wing will be used to carry out a finite element analysis on the wing structure.

53

4.2   Main Wing Structure Performance

A wing under operating conditions experiences aerodynamic loads. These aerodynamic loads will be used to conduct a structural analysis on the main wing structure of the Stop-Rotor UAV. For this structural analysis it is assumed that the wing is made out of Aluminum 2014, which has Young Modulus of 9.53E6 psi and a Poisson's ratio of 0.33. The wing will be pinned supported at two bearing locations at the aluminum spar. The loads that the wing structure will be subjected to are lift force, drag force, and moment. All aerodynamic loads will be assumed to be acting at quarter chord point and to be constant along span of the wing.

The first step in conducting this analysis was to determine the aerodynamic loads that the wing structure would experience. These loads were determined by conducting a 2-D CFD analysis on a NACA 0012 airfoil. The calculated Reynolds number the wing would operate was 483,908 at STP. The CFD analysis was conducted using XFLR5 software. In doing the CFD analysis, coefficients of lift, drag, and moment were obtained at various angles of attack.

Table 4.1

Coefficient of Lift, Drag and Moment at different angles of attack

Alpha	C_L	C_D	C_M
0°	0	0.0062	0
5°	0.631	0.0105	-0.0134
10°	1.041	0.0196	0.0114
15°	1.219	0.0499	0.0331

Once obtaining these coefficients, the aerodynamic forces were calculated using the following equations:

$$L = C_L \cdot \frac{1}{2} \cdot \rho \cdot V^2 \cdot S$$

$$D = C_D \cdot \frac{1}{2} \cdot \rho \cdot V^2 \cdot S \qquad\qquad (4.1)$$

$$M = C_M \cdot \frac{1}{2} \cdot \rho \cdot V^2 \cdot S \cdot c$$

where, S is the plan-form area and the span assumed to be one, c the chord length,

ρ the air density, and V free stream velocity.

Table 4.2

Aerodynamic loads at different angles of attack

Alpha	Lift per unit Span (N/m)	Drag per unit Span (N/m)	Moment per unit Span (Nm)
0	0	0.72	0
5	72.97	1.21	-0.41
10	120.27	2.26	0.35
15	140.86	5.76	1.02

The next step was to construct the wing structure using Solidworks. The

structure consisted of two major components, an airfoil skin and the aluminum

spar. The span of the wing was 47.5 inches and the thickness was assumed to be

0.1 inches. The aluminum spar had a span of 52.5 inches and the thickness of the

aluminum spar was measured to be 0.125 inches. The material for both
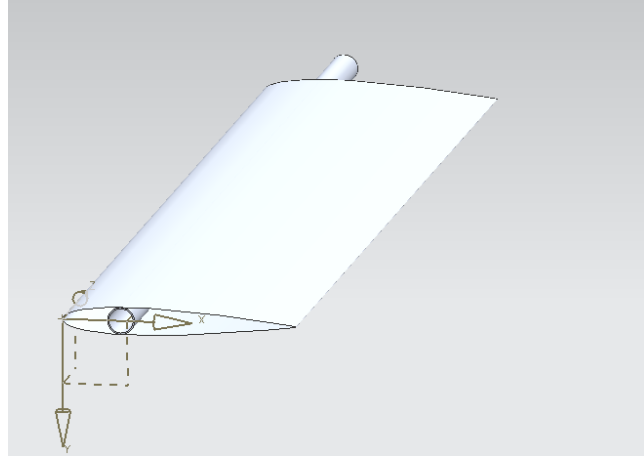
components was assumed to be Aluminum 2014.

Figure 4.7. **Wing structure**

The wing structure was then inputted into NX 7 Nastran where a mesh, constraints, and loads were applied. The elements selected for this analysis were thin shell Quad-4, and solid Hex-8. The airfoil skin used the thin shell while the aluminum spar used solid elements. A 2-D mapped mesh was applied on the airfoil skin while a 3-D swept mesh was applied on the aluminum cross section. This resulted in a uniform mesh in the aluminum spar and airfoil. A face split was used on the top surface of the airfoil to create a single contact point with the aluminum spar. At this location the spar and airfoil shared common nodes along the span wise direction.
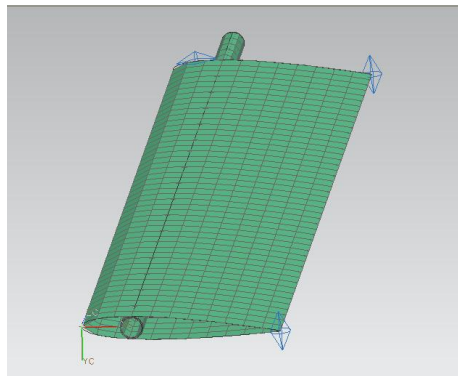

Figure 4.8. **Mesh of wing structure**

The last step to setting up the analysis was to input the loads and constraints. The edge created by the face split was used to apply the lift and drag forces. The lift force was applied on the top surface of the airfoil skin in the negative y-direction, while the drag force was split in half and applied in the top and bottom of the spar in the x-direction. The moment was applied in the inner surface of the tube in the z-direction.

The constraints used for this analysis were pinned constraints at the aluminum spar. These constraints were selected to simulate the mounting structure of the wing. The method of applying these constraints was using a user defined constraint. This was done by fixing the translations in the x, y, and z direction in selected nodes at the locations where the bearing supports would be located.
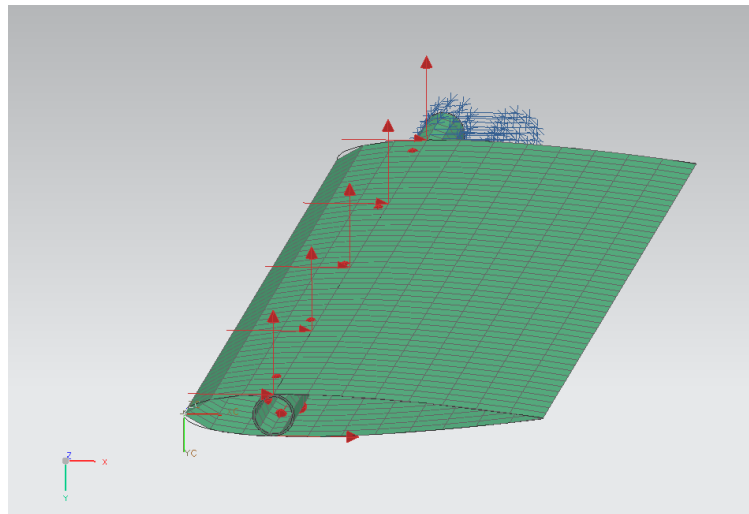

Figure 4.9. **Loads and constraints**

For this structural analysis the results obtained were for deflection, Von Mises stresses, and vibration of the wing structure. This analysis was conducted using the maximum values of lift, drag, and moment forces previously obtained.

The wing structure had a maximum magnitude deflection of 0.167 inches located at the tip of the wing. The minimum deflection was 0 inches situated at the constraints.
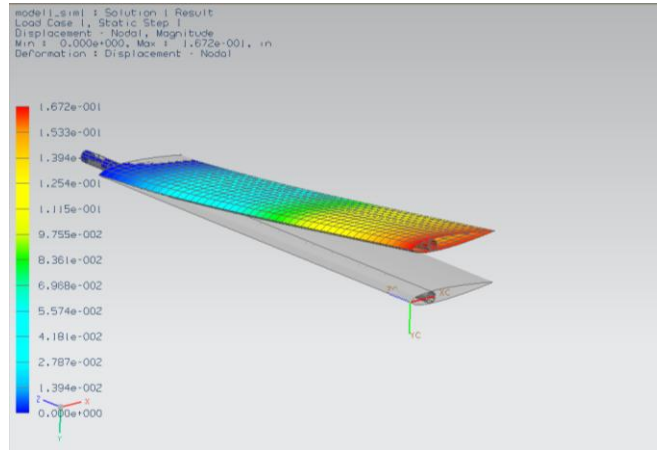

Figure 4.10. **Magnitude deflection of wing structure**

The maximum and minimum deflection in the x and y directions are given in the following table:

Table 4.3

Max. and min. deflection in x and y direction

Direction	Maximum	Minimum
X-direction	0.0022 in.	-0.00029 in.
Y-direction	0.167 in.	-0.00675 in.

The results obtained in the simulation appear to be accurate, because the model had the most deflection in y-direction. This makes sense since the lift force was the main force acting on the wing, with 140.86 N/m while drag and moment only applied 5.76 N/m and 1.02 Nm. The behavior of the deflection is reasonable, even though the wing structure did not behave in a cubic way, shown in the Figure 4.11.
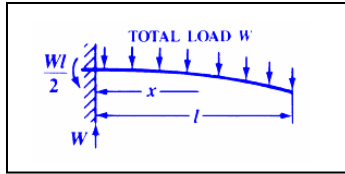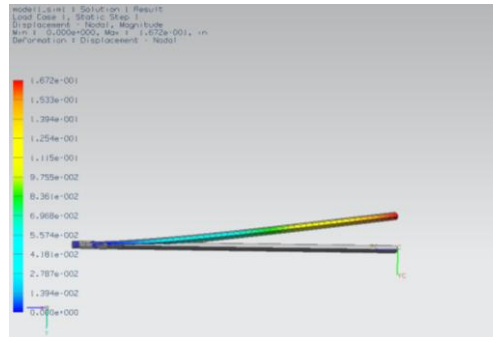
Figure 4.11. **Deflection with cubic behavior**

Figure 4.12. **Deflection of model with linear behavior**

The model behaved linearly from the point that the airfoil skin and the spar joined

together. This is due to the fact that after the constraints the spar had an added

stiffness that was provided by the airfoil skin. So deflection was constant.

The maximum Von-Mises stress was obtained to be 5,421 psi located next

to the pinned constraint, while the minimum Von-Mises stress was 1.931 psi at
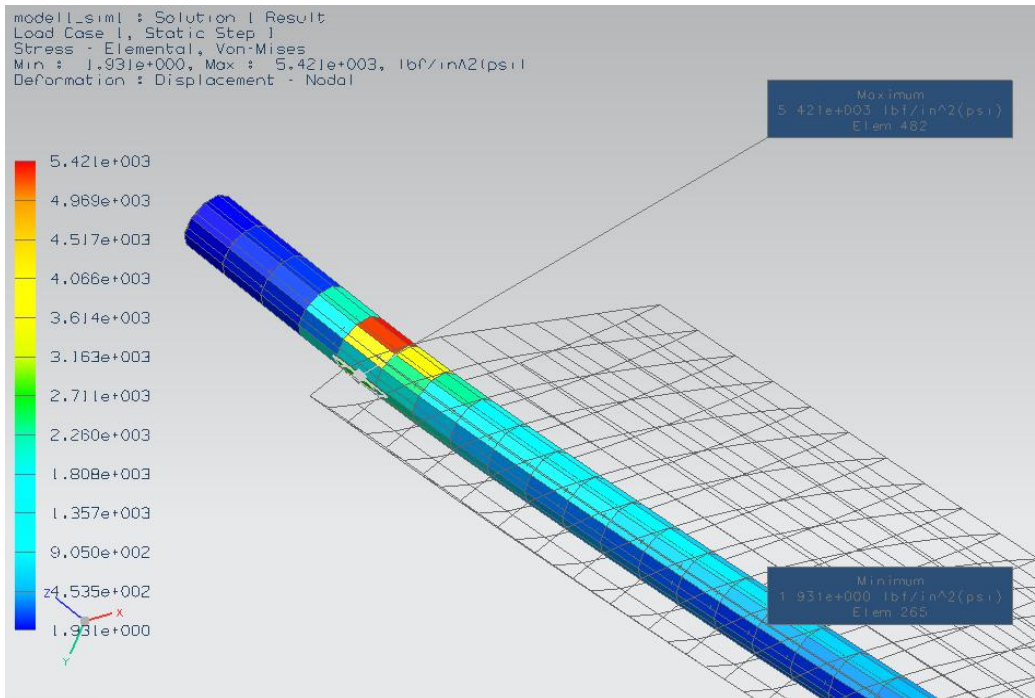
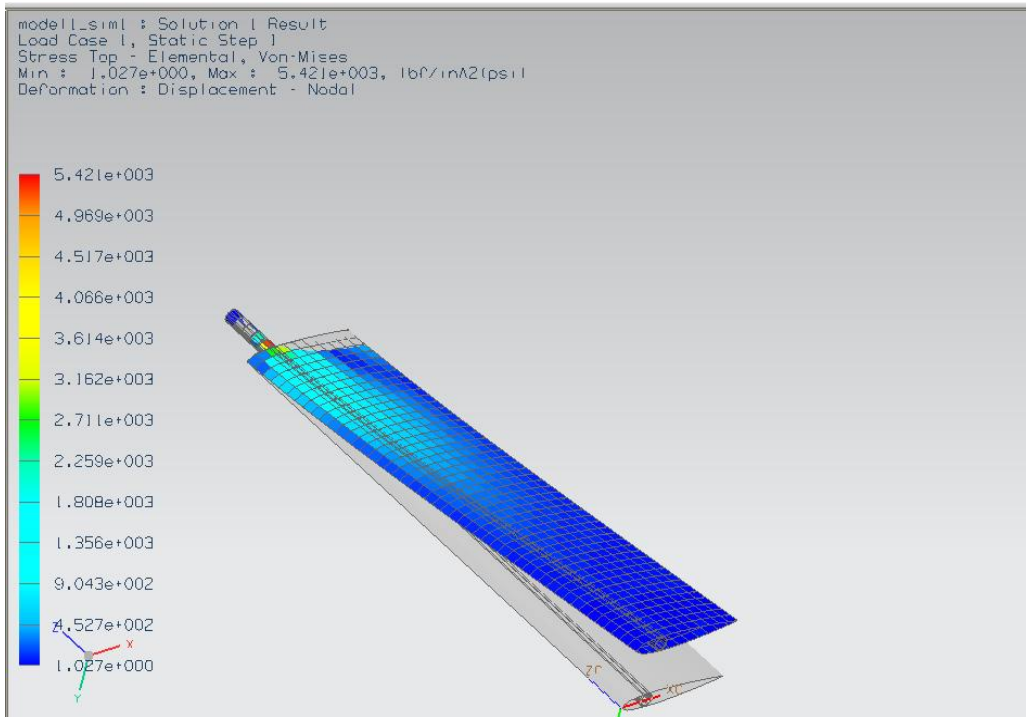the tip of wing.

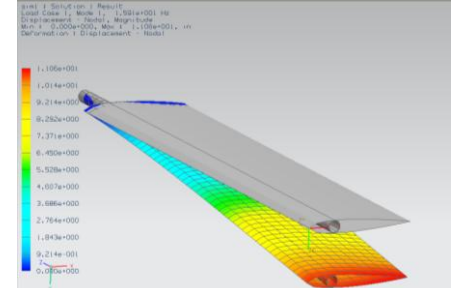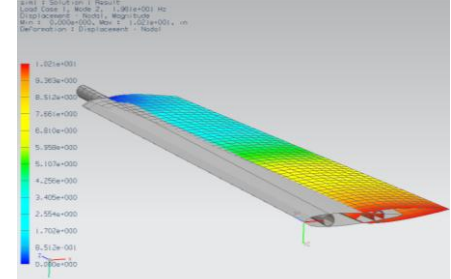***Figure 4.13.*** **Maximum Von Mises stress**

***Figure 4.14.*** **Von Mises stress in entire wing structure**

The maximum Von-Mises stress occurred at the bottom and top of the spar right

after the constraints, this is understandable since the wing structure is mostly

experiencing a bending due to the lift. As well, the maximum stress 5,421 psi is

well within the yield strength of Aluminum 2014 which is 60,000 psi (ASM,

2001). This relative low Von-Mises value is due to the weak loading conditions

the structure experienced. The aerodynamic forces were calculated using the

assumption the max. velocity the wing would experience was 26.82 m/s, which is

a qualified small velocity. So the aerodynamic forces were small.

Lastly, for the structural analysis vibrations results at various frequencies

were obtained.

Table 4.4

Vibration deformations at various mode

Vibration Frequency	Deformation Type
Mode 1: 15.9 Hz	
Mode 2: 19.6 Hz	

Mode 3: 71 Hz	
Mode 4: 112.5 Hz	
Mode 5: 168.3 Hz	
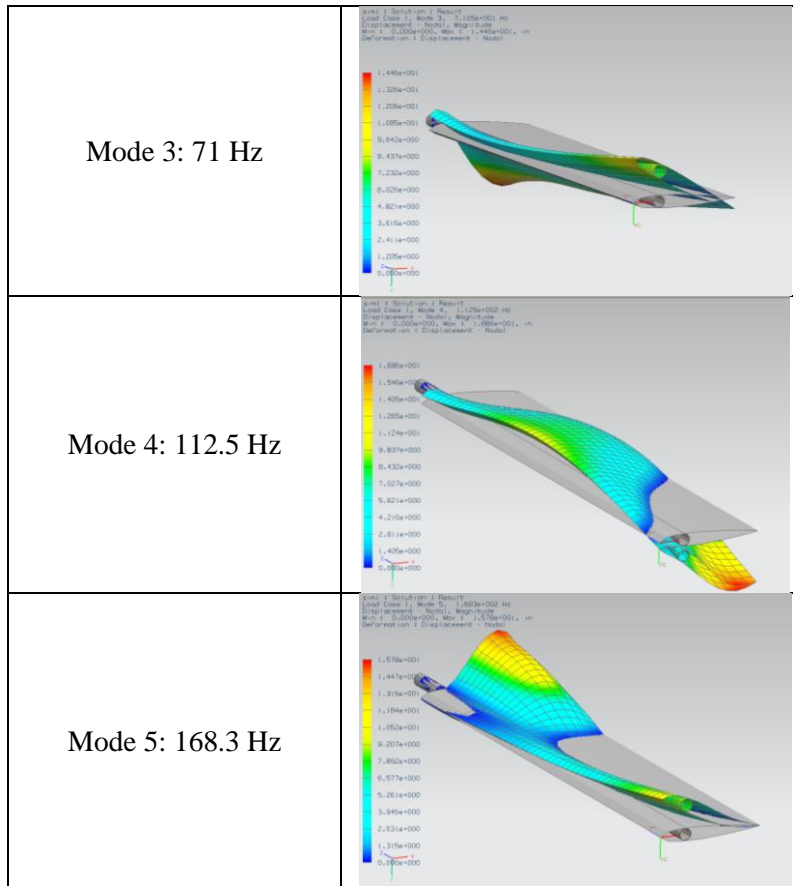
The results obtained from vibration are realistic because it illustrated all of the

deformations that are expected under vibration. Usually a model under vibration

exhibits the following behaviors:

Table 4.5

Vibration deformations

Vibration Mode	Deformation Type
Mode 1	Bending
Mode 2	Lead or Drag
Mode 3	Torsion
Mode 4	Second Bending
Mode 5	Second Torsion

The structure exhibited exactly same deformations as the expected ones. These

deformations can be seen in Table 4.4.

Upon concluding the structural analysis accurate results for deflection, Von-Mises stresses and vibration were obtained. These results are an excellent stepping point to conduct additional structural analysis on wing mount structure, though further improvements and modifications can be applied to obtain results with greater degree of accuracy. Some recommendations are to use smaller elements, obtain more realistic aerodynamic loads, and improve the application of those loads to the structure.

Chapter 5

CONCLUSIONS

In this work, design and analysis of a multimode Stop-Rotor UAV is presented. This axial flow stop-rotor is capable of VTOL with ability to transition from helicopter to airplane mode and vice versa in flight.

A mathematical model was developed that captures the stop-rotor dynamics in hover. It is noted that the stop rotor is unstable in hover. So a linear, Linear Quadratic Regulator (LQR) control was designed and implemented to stabilize the hover dynamics. This linear control works when the initial conditions are small and nonlinear effects are not significant. The linear control achieves 'local' stability and may not work for all large disturbances or initial conditions. In order to ensure 'global' stability a Lyapunov approach based nonlinear controller was designed and implemented on the nonlinear plant. The domain of attraction for this nonlinear controller is much higher than the linear controller. Furthermore, the control robustness was discussed.

An experimental validation 'big drop' test was also conducted in which an unpowered stop-rotor specimen was dropped from a hot air balloon. This specimen successfully demonstrated transition from the helicopter to airplane mode. During the test, crucial experimental rotor RPM data was obtained which was then compared to a simple mathematical model. Preliminary equations for helicopter to airplane transition via pitch control were also derived. It is noted that during drop 'pitch control' via RC transmitter was utilized to pull the aircraft from helicopter mode.

Finally, performance of the Stop-Rotor UAV in fixed-wing mode was studied. Primarily, the stability of the aircraft was determined, which served for consideration for future changes in the stop-rotor's design. In evaluating the aircraft performance, it was apparent that for future aircraft performance analysis required software that had more competence. Lastly, design considerations were considered on the main wing structure. This allowed for the evaluation of the main wing performance in fixed-wing flight.

It is anticipated that this work would serve as the foundation to develop a complete autonomous multimode Stop-Rotor UAV. The future work can include simulating the transition equations, design controller for transition dynamics and detailed mathematical analysis that relaxes the assumptions that were used while deriving the equations of motion, to mention a few.

REFERENCES

C. Anderson. (2010). Ardupilot. Retrieved (July 2010) from:
        http://diydrones.com/notes/ArduPilot

J. D. Anderson. (1999). Aircraft performance and design, 5, 252-255. (ISBN:
        9870070019713)

ASM aerospace specification metals inc. (2001). Retrieved (March 2010) from:
        http://asm.matweb.com/search/SpecificMaterial.asp?bassnum=MA2014T6

Z. Bai, J. Demmel, J. Dongarra, A. Ruhe, H. Van Der Vorst. (2000). Generalized
        Hermitian Eigenvalue Problems: Templates for the Solution of Algebraic
        Eigenvalue Problems. A Practical Guide Philadelphia:
        SIAM. ISBN: 0898714710

J. S. Bay. (1999). Linear state space systems, 7, 280-285. (ISBN: 0256246394)

J. E. Bertram, R. E. Kalman. (1960). Control system and analysis and design via
        the second method of Liapunov: Parts I and II, Journal of Basic
        Engineering, Vol 82, pp. 371-400.

S. Bouabdallah. VTOL aircraft dynamic modeling of MAVS. Retrieved (January
        2010) from: www.asl.ethz.ch/education/.../2010-L6-
        Dynamic_Modeling_Rotorcraft.pdf

W. L. Brogan. (1974). Modern Control Theory. Quantum Publishers, New York.

B. Brown. (1922). Chinese Nights Entertainments, Brentano's, OCLC 843525

J. B. Burl. (1999). Linear optimal control: H2 and H(infinity) methods. Addison
        Wesley Longman, New York

P. Castillo, A. E. Dzul, R. Lozano. (2005). Modelling and control of mini-flying
        machines. 5, 85-94. (ISBN: 1852339578)

A. Vargas-Clara, S. Redkar. (2010). Development of a stop-rotor unmanned aerial
        vehicle. Proceedings of the 2011 IAJC-ASEE international conference
        (ISBN: 9781606433799)

T. Crouch, (2004). Wings: A History of Aviation from Kites to the Space Age,
        New York, New York: W.W. Norton & Co, ISBN 0393326209

A. Deporris. (2010). Why do I get the message. Retrieved (May 2011) from:
        xflr5.sourceforge.net/docs/Point_Out_Of_Flight_Envelope_fr.pdf

M. Drier. (2007). Introduction to helicopter and tiltrotor flight simulation, 11, 236-237. (ISBN: 1563478730)

F.R. Gantmacher. (1977). The theory of matrices. Chelsea Publishing Co. New York

E. F. Infante. (1968). On the stability of some linear non-autonomous random systems', J. Appl. Mech. 35, 7-12. Retrieved (June 2011)

F. Kozin. (1986). Some Results on stability of Stochastic Dynamical Systems. Probabalistic Enginering Mechanics. Vol 1 (1), pp 13- 22

F. Meschia. (2008). Model analysis with XFLR5. Radio control soaring digest. Vol. 25, No. 2. Retrieved (May 2011) from: http://www.rcsoaringdigest.com/pdfs/RCSD-2008/RCSD-2008-02.pdf

S. R. Osborne. (2007). Transition between hover and level flight for a tailsitter UAV. Retrieved (May 2011) from: http://contentdm.lib.byu.edu/ETD/image/etd2054.pdf

XFLR5. Retrieved (March 2010) from: http://xflr5.sourceforge.net/xflr5.htm